# Impacts of El Niño events on the Peruvian upwelling system productivity

**D. Espinoza-Morriberón[1,2]** [ID], **V. Echevin[2]**, **F. Colas[2]** [ID], **J. Tam[1]**, **J. Ledesma[1]**, **L. Vásquez[1]**, and **M. Graco[1]**

[1]Laboratorio de Modelado Oceanográfico, Ecosistémico y de Cambio Climático (LMOECC)/Instituto del Mar del Peru (IMARPE), Esquina general Gamarra y Valle, Callao, Peru, [2]Laboratoire d'Océanographie et du Climat: Expérimentations et Approches Numériques (LOCEAN), IRD/Sorbonne Universites (UPMC Univ Paris 06)/CNRS/MNHN, 4 Place Jussieu, Paris Cedex, France

**Abstract** Every 2–7 years, El Niño events trigger a strong decrease in phytoplankton productivity off Peru, which profoundly alters the environmental landscape and trophic chain of the marine ecosystem. Here we use a regional coupled physical-biogeochemical model to study the dynamical processes involved in the productivity changes during El Nino, with a focus on the strongest events of the 1958–2008 period. Model evaluation using satellite and in situ observations shows that the model reproduces the surface and subsurface interannual physical and biogeochemical variability. During El Niño, the thermocline and nutricline deepen significantly during the passage of coastal-trapped waves. While the upwelling-favorable wind increases, the coastal upwelling is compensated by a shoreward geostrophic near-surface current. The depth of upwelling source waters remains unchanged during El Niño but their nutrient content decreases dramatically, which, along with a mixed layer depth increase, impacts the phytoplankton growth. Offshore of the coastal zone, enhanced eddy-induced subduction during El Niño plays a potentially important role in nutrient loss.

## 1. Introduction

The Peru upwelling system (also known as the Northern Humboldt Current System) is one of the most important coastal upwelling systems of the global ocean [*Chavez and Messié*, 2009; *Lachkar and Gruber*, 2012]. Along the coasts of Peru, equatorward winds drive a persistent coastal upwelling of cold and nutrient-rich waters, triggering a high primary productivity [e.g., *Tarazona and Arntz*, 2001; *Pennington et al.*, 2006]. This high productivity supports diverse and abundant fisheries, particularly the Peruvian anchovy [*Chavez et al.*, 2008]. The features of the Peruvian upwelling system are dramatically impacted at interannual time scales by the El Niño-Southern Oscillation (ENSO).

During El Niño (EN), the warm phase of ENSO, a weakening of the trade winds over the equatorial Pacific allows the eastward displacement of West Pacific warm pool [*Picaut et al.*, 1996], generating positive sea surface temperature (SST) anomalies in the Central and Eastern Pacific Ocean. Environmental conditions off Peru change dramatically: SST strongly increases (e.g., $\sim +3°C$ SST anomaly in 1997–1998) [*Picaut et al.*, 2002], ventilated and nutrient-depleted waters are found near the coast [*Arntz et al.*, 2006; *Graco et al.*, 2007, 2016], and surface chlorophyll decreases (e.g., $\sim -4$ mg.m$^{-3}$ anomaly during the extreme 1997–1998 EN) [*Thomas et al.*, 2001; *Carr et al.*, 2002; *Calienes*, 2014]. The planktonic biomass decrease during EN triggers habitat changes and high mortality for several fish populations such as the Peruvian anchovy [*Alheit and Ñiquen*, 2004; *Ñiquen and Bouchón*, 2004] but also for top predators due to reduced food availability [*Tovar and Cabrera*, 1985]. One should keep in mind that the impact of a given EN event on the Peru ecosystem depends on its intensity and spatial structure: the so-called "central Pacific" EN events [e.g., *Takahashi et al.*, 2011] are not likely to have a strong impact near the Peruvian coast in contrast with the "Eastern Pacific" EN events (e.g., 1997–1998).

A pronounced bottom-up mechanism happens during EN owing to the decrease of primary producers [*Tam et al.*, 2008]. The lowest chlorophyll concentrations (a proxy for the phytoplankton biomass) near the coast of Peru in the last 50 years were observed during extreme 1982–1983 and 1997–1998 EN events [*Calienes*, 2014; *Gutiérrez et al.*, 2016]. In climatological conditions, surface chlorophyll off Peru peaks in summer ($\sim 4$ mg.m$^{-3}$) and spring ($\sim 2$ mg.m$^{-3}$) [*Echevin et al.*, 2008]. In contrast, during the 1983 EN chlorophyll-*a*-

poor waters ($<0.3$ mg.m$^{-3}$) were observed north of 14°S [*Calienes*, 2014], and values of 0.5–1 mg.m$^{-3}$ were recorded along the coast of Peru during the 1997–1998 EN [*Carr et al.*, 2002]. These waters were associated with low nutrient concentrations near the surface [*Barber and Chavez*, 1983].

Different physical processes can have an impact on the productivity of the upwelling system during EN:

1. Intense downwelling equatorial Kelvin waves [e.g., *Kessler and McPhaden*, 1995] trigger coastal trapped waves (CTW) which deepen the nearshore thermocline/nutricline [e.g., *Barber and Chavez*, 1983; *Calienes*, 2014; *Echevin et al.*, 2014; *Graco et al.*, 2016].
2. Changes in equatorial circulation and nutrient concentrations of the upwelling source water (SW) occur during EN. The Peru-Chile Undercurrent (PCUC), a major source water for the Peru upwelling [*Huyer et al.*, 1991; *Albert et al.*, 2010], is fueled by the zonal, eastward Equatorial Undercurrent (EUC) [*Wyrtki*, 1967] and mainly by the Subsurface countercurrents (SSCCs) [*Tsuchiya*, 1975; *Montes et al.*, 2010]. During EN, the position and intensity of the latter are modified [*Montes et al.*, 2011], which may produce changes in the subsurface circulation, water masses, and hence nutrient flux to the upwelling system.
3. Last, mesoscale eddies of higher intensity have been observed during EN [*Chaigneau et al.*, 2008]. This enhanced eddy activity could increase the offshore transport and subduction of nutrients and plankton [*Lathuilière et al.*, 2010; *Gruber et al.*, 2011; *Thomsen et al.*, 2016].

During the cold phase of ENSO (La Niña, LN), the Peru ecosystem is less impacted: upwelling-favorable winds off Peru are intensified, resulting in negative SST anomalies [*Morón et al.*, 2000] and a slightly higher phytoplankton and anchovy biomass [*Calienes*, 2014; *Bouchón and Peña*, 2008].

The main goal of the present study is to investigate the previously mentioned mechanisms and discuss their respective impacts on phytoplankton growth during EN, using a regional physical-biogeochemical coupled model. For this purpose, the 1958–2008 period, which includes several EN events and in particular the extreme 1982–1983 and 1997–1998 events, was simulated. While the study focused on EN events, impacts of LN events are also briefly presented. In the following, we describe the data, model configuration and methods in section 2. Results evaluating the model realism and the main processes at play during EN events are described in section 3. The respective processes that produce the chlorophyll decrease are discussed in section 4. The main conclusions and perspectives of this study are presented in section 5.

## 2. Material and Methods

### 2.1. The Coupled Physical-Biogeochemical Model
#### 2.1.1. Model Characteristics
The Regional Oceanic Modeling System (ROMS) resolves the Primitive Equations, based on the Boussinesq approximation and hydrostatic vertical momentum balance. A third-order, upstream-biased advection scheme allows the generation of steep tracer and velocity gradients [*Shchepetkin and McWilliams*, 1998]. For a complete description of the model numerical schemes, the reader is referred to *Shchepetkin and McWilliams* [2005]. The model is used here in its "AGRIF ROMS" version [*Shchepetkin and McWilliams*, 2009].

The Pelagic Interaction Scheme for Carbon and Ecosystem Studies (PISCES) simulates the marine biological productivity and the biogeochemical cycles of carbon and main nutrients (P,N,Si,Fe) [*Aumont and Bopp*, 2006; *Aumont et al.*, 2015]. PISCES has three nonliving compartments which are the semilabile dissolved organic matter, small-sinking particles, and large-sinking particles. It has four living compartments represented by two size classes of phytoplankton (nanophytoplankton and diatoms) and two size classes of zooplankton (microzooplankton and mesozooplankton). The growth of phytoplankton is limited by external nutrients concentration and diatoms differ from nanophytoplankton by their need for silicate and higher iron requirements [*Sunda and Huntsman*, 1997]. Zooplankton feeds on two phytoplankton sizes and their predators are implicitly parameterized by a linear and a quadratic mortality term simulating the predation of an infinite chain of carnivores [*Buitenhuis et al.*, 2006]. The reader is referred to *Aumont et al.* [2015] for a complete description of the model, and to *Echevin et al.* [2014] for a list of biogeochemical parameters values used in the Peru upwelling system.

#### 2.1.2. Model Configuration
The model domain extends from 15°N to 40°N and from 100°W to 70°W. The domain encompasses the Northern and central Chile region; however, our analysis focused on the Peruvian coastal region (Figure 1).
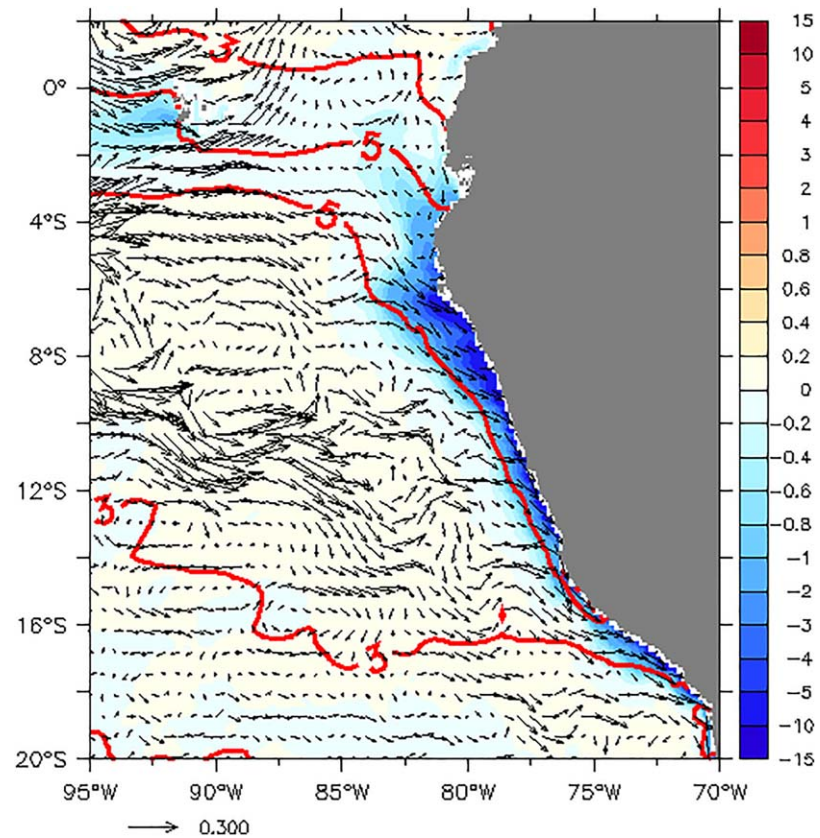
**Figure 1.** Surface velocity anomalies (arrows, in m.s$^{-1}$), surface chlorophyll anomalies (color scale, in mg.m$^{-3}$), and sea surface temperature anomalies (red lines marking +3 and +5°C) in December 1997 to March 1998 for the simulation. Anomalies were computed with respect to the 1958–2008 climatology.

The horizontal resolution of the grid is 1/6°, corresponding to ~18.5 km. The bottom topography from ETOPO2 [*Smith and Sandwell*, 1997] is interpolated on the grid and smoothed in order to reduce potential error in the horizontal pressure gradient. The vertical grid has 32 sigma levels.

### 2.1.3. Open Boundary Conditions

Open boundary conditions (OBC) for physical variables (temperature, salinity, velocities, and sea-level) came from an interannual SODA model solution (version 2.1.6) [*Carton and Giese*, 2008] which has a horizontal resolution of 0.5° and 40 vertical levels. Five day-averaged outputs are used for the period 1958–2008. SODA-assimilated hydrographic profiles, moored and satellite data. It was forced with ECMWF ERA-40 atmospheric fluxes [*Uppala et al.*, 2005].

OBC for biogeochemical variables came from CARS2009 climatological data [*Ridgway et al.*, 2002] with a horizontal resolution of 0.5° and 79 vertical levels for oxygen and nutrients (nitrate, phosphate, silicate) and from World Ocean Atlas climatology (WOA2005) [*Conkright et al.*, 2002] for dissolved organic carbon (DOC), dissolved inorganic carbon (DIC), and total alkalinity (TALK). The DIC and TALK from WOA do not have seasonal variation. Iron came from a NEMO-PISCES global simulation climatology [*Aumont and Bopp*, 2006].

### 2.1.4. Regional Atmospheric Forcing

Statistically downscaled NCEP interannual monthly wind anomalies [*Goubanova et al.*, 2011] and SCOW monthly climatological winds [*Risien and Chelton*, 2008] were added to construct surface wind fields. NCEP monthly anomalies and COADS monthly climatology [*Da Silva et al.*, 1994] were added to construct short wave heat flux and surface air parameters used in ROMS bulk parameterization [*Liu et al.*, 1979].

The atmospheric forcing fields, physical and biogeochemical initial and open boundary conditions were interpolated onto the ROMS grid using the ROMSTOOLS preprocessing package [*Penven et al.*, 2008].

To remove trends induced by the adjustment of the model to initial and boundary conditions, a 20 year spin-up in climatological mode was first run. We used a monthly climatological forcing derived from the

atmospheric forcing and monthly climatological OBC from the 5 day SODA OBC. These monthly climatologies were computed over the period 1958–1970. Statistical steady state was reached for physical variables and biogeochemical variables after 3 and 20 years, respectively. Steady state was used as initial condition (1 January 1958) to run the ROMS-PISCES model. The model was run from 1958 to 2008 and the outputs are stored as 5 day averages.

### 2.2. Lagrangian Analysis

The ROMS-offline tracking module [*Capet et al.*, 2004] was used to calculate the trajectories of water parcels. The virtual float trajectories were computed using the 5 day-averaged ROMS velocity fields. Floats register nitrate and iron concentrations along their trajectories. Two experiments were made to study the properties of the upwelling source water (SW): SW were tracked back 1 month before they were upwelled near the coast, and when they were located in the equatorial zone during LN, neutral, and EN conditions.

In the first experiment, to study the pathways and the characteristics of the SW, 10,000 floats were released every first day of each month from 1958 to 2008 in the surface layer (between 0 and 15 m depth), between the coast and the 100 m isobath in the latitude range 6°–14°S. The floats were then tracked backward in time during 1 month after they had left the mixed layer. In our statistical analysis, we did not take in account the floats that left the mixed layer more than 1 month after being released. From all these floats characteristics, we computed a climatology of the SW depth and nitrate concentration one month before they were upwelled.

In the second experiment, we used the same criterion to select the floats which were tracked backward in time during 2 years. The floats reaching 88°W between 2°N and 10°S (e.g., the typical latitude range of the EUC and SSCCs) [*Montes et al.*, 2010] were used to compute statistics of the SW properties in the equatorial region. In this experiment the floats were released in spring (October, November, December) during every LN, neutral, and EN event.

To compute a probability of presence for a specific depth or concentration range and for a specific month, we counted the particles in the given range and divided this number by the total number of particles upwelled during that month.

### 2.3. Satellite Data Sets

Monthly mean sea surface temperature from Pathfinder satellite data ($\sim$4 km) [*Casey et al.*, 2010] over the period 1984–2008 were used to evaluate SST over the entire model domain. AVISO satellite altimetry data (www.aviso.oceanobs.com) from January 1993 to December 2008 (every 5 days) were used to evaluate the model sea level variability. The 1/3° gridded data were interpolated onto the model grid. Besides, monthly SeaWIFs satellite data [*OReilly et al.*, 1998] at 1/12° ($\sim$9 km) resolution were used to validate the model surface chlorophyll concentration from September 1997 to December 2008.

### 2.4. In Situ Data Sets

Temperature, nitrate, and chlorophyll-*a* (hereafter Chl) data from IMARPE (Instituto del Mar del Peru) sampling were gridded vertically (every 10 m) and then horizontally at the same resolution (1/6°) as the model. Extreme values (in log scale for Chl) were filtered out by removing values higher than twice the standard deviation in each bin. For more details on the Chl and nitrate measurement protocols, the reader is referred to the appendix in *Echevin et al.* [2008]. IMARPE cruises are generally planned twice a year with some exceptions. Gridded (1/2° resolution) surface nitrate concentration from CARS [*Ridgway et al.*, 2002] was also used to evaluate the nitrate concentration model.

### 2.5. Cross-Shore Sections and Coastal Indices

Alongshore-averaged vertical sections for neutral and EN periods are computed to highlight the mean cross-shore structures. We averaged data between 6°S–16°S and 100 km from the coast (Figure 1; hereafter coastal region), which encompasses most of the IMARPE data.

Due to a subsurface temperature and nitrate bias, thermocline and nutricline depth (hereafter ZT and ZNO$_3$) were defined as follows: ZT was the depth of the 15°C and 16°C isotherm in IMARPE and model, respectively, and ZNO$_3$ was the depth of the 16 $\mu$mol.L$^{-1}$ and 21 $\mu$mol.L$^{-1}$ nitrate isoline in IMARPE and model, respectively. ZT, ZNO$_3$, and surface Chl were averaged in the coastal region (see green line in Figure 1) every 6 months to define coastal indices. In order to compute ZT and ZNO$_3$, the IMARPE profiles of temperature

and nitrate were linearly interpolated on a vertical grid with a 1 m resolution. The coastal SST anomalies were computed every month because of their higher sampling in space and time.

To illustrate the data scarcity, we computed for a given variable $X$ an index of Sample Representation ($ISR(x)$) over the Peruvian coastal region: $ISR(x) = |100 * (1 - X_s/X_c)|$, where $X_s$ represents the spatial mean of the model variable sampled using the positions of observational data and $X_c$ represents the spatial mean of the model variable using all the model grid points in the region of averaging. The coverage ratio was computed as $N_{sampled}/N_{total}$, where $N_{sampled}$ represents the number of grid points with observations and $N_{total}$ is the total number of grid points in the coastal band ($N_{total} = 438$ points).

### 2.6. Eddy Subduction During EN

In order to filter the nearshore influence of the CTW and focus on the mesoscale processes related to the formation of eddies and filaments, the eddy kinetic energy ($EKE_m$) was computed in an offshore band (between 100 and 500 km from the coast and 6°S–14°S). A 60 days moving average filter (labeled $<.>$ in the following) was applied to zonal ($<u>$) and meridional ($<v>$) currents, to compute mesoscale anomalies $u' = u - <u>$ and $v' = v - <v>$. The equation for $EKE_m$ is defined as follows: $EKE_m = \frac{(u')^2 + (v')^2}{2}$.

In order to evaluate nitrate subduction during EN, we estimate the nitrate vertical eddy flux:

$$\overline{w'.N'} = \overline{w.N} - \overline{\langle w \rangle . \langle N \rangle}$$

where w and $N$ are 5 day-averaged vertical velocity and nitrate concentration, respectively, $<w>$ and $<N>$ represent the 60 day filtered values of $w$ and $N$, and $w'$ and $N'$ are the eddy terms. The overbar represents a spatial average over an offshore band located 100–500 km from the coast and between 6°S and 14°S. We computed the eddy terms every 5 m from 0 to 250 m depth and averaged them for EN and neutral periods.

### 2.7. Definition of EN Periods

An EN (LN) period is defined when the 3 month-running mean SST anomaly in the Niño 1 + 2 region (0–10°S and 90°W–80°W) is larger (less) than +0.5°C (−0.5°C) for at least five consecutive months, using ERSST.v4 data [*Huang et al.*, 2015]. Neutral periods occur during non-EN and non-LN periods. In addition, we defined different categories of EN events. If the SST anomalies are greater than +1.6°C during at least 3 months the event is considered an "extreme" EN otherwise it is a "moderate" EN. The correlation between model and observed EN 1 + 2 index was 0.9 and both indices detected three EN extremes (1972–1973, 1982–1983, and 1997–1998), and the majority of the EN moderates. Note that in the model solution, the 2002 EN appears as a warm period presenting only 4 months with SST anomalies greater than +0.5°C.

## 3. Results

### 3.1. Model Evaluation
### 3.1.1. Surface Mean State

We compared the mean modeled and observed surface patterns of temperature, nitrate, and Chl (Figure 2). Coastal waters were colder than offshore in the model and observations (Figures 2a–2c) because of the upwelling of subsurface waters. Between 13°S and 16°S, the coldest coastal waters associated with the intense Pisco upwelling (∼13.5°S) [*Gutiérrez et al.*, 2011] were seen in both the observations (∼16–17°C in IMARPE and ∼18°C in Pathfinder) and the simulation (∼18°C).

The surface nitrate distribution presented high concentrations near the coast due to the persistent coastal upwelling which brought nutrient-replete subsurface waters to the surface, especially in two regions between 4°S–6°S and 14°S–16°S (Figures 2d–2f). The model reproduced the maximum nearshore nitrate concentrations and overestimated the observed values by ∼5 $\mu mol.L^{-1}$ (Figure 2f).

The surface Chl concentration presented a marked contrast between the coastal region and the open ocean. The coastal region averaged value was ∼4.2 $mg.m^{-3}$ in SeaWIFS, ∼3.6 $mg.m^{-3}$ in IMARPE, and ∼4.9 $mg.m^{-3}$ in the model, while low values (<1 $mg.m^{-3}$) were encountered offshore (>200 km). The richest nearshore areas (>5 $mg.m^{-3}$) off Peru were located between 8°S and 12°S in IMARPE (Figure 2g), 11°S and 14°S in SeaWIFS (Figure 2h), and between 6°S and 14°S in the simulation (Figure 2i). Computed over the SeaWIFS period (1997–2008), the model coastal average was higher (∼6.4 $mg.m^{-3}$) than over the 1958–2008 period. Overall, the nearshore productivity was overestimated by the model, in particular between 6°S
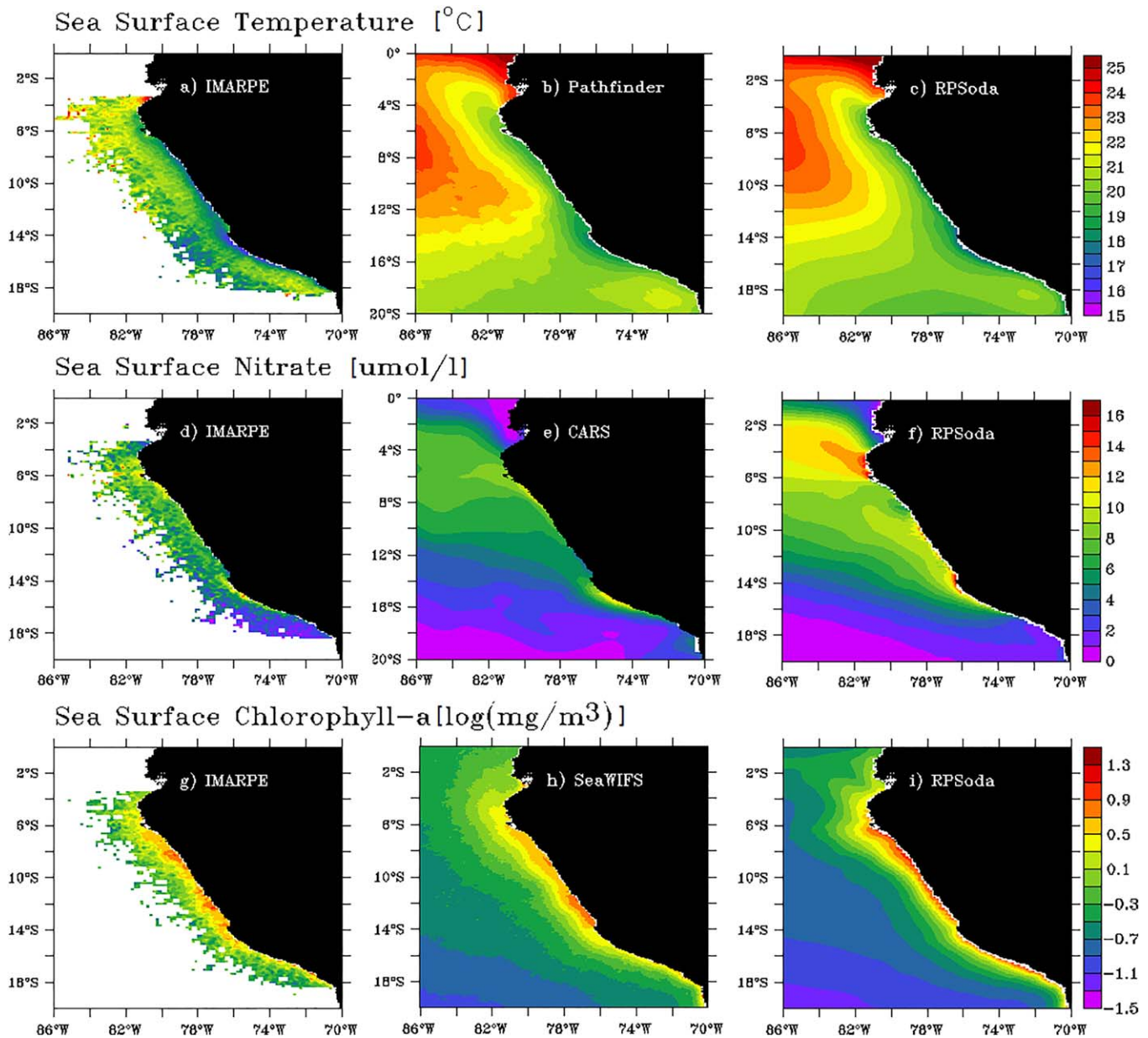
**Figure 2.** (a–c) Mean sea surface temperature (°C), (d–f) surface nitrate concentration (μmol.L$^{-1}$), and (g–i) surface chlorophyll (mg.m$^{-3}$) for observational data and model simulation. IMARPE data were averaged between 1965 and 2008, SeaWIFS data were averaged between 1997 and 2010.

and 10°S and south of 14°S (Figure 2h), probably due to the model high subsurface nitrate concentrations (Figures 2d–2f).

The modeled seasonal cycle of surface Chl was also evaluated in the coastal region (supporting information Figure S1a). Model and observations peaked during late spring-summer, and displayed low values during winter. The model solution overestimated surface Chl by ∼4 mg.m$^{-3}$ (75%) during late spring-summer and by ∼2 mg.m$^{-3}$ (90%) during the rest of the year with respect to SeaWIFS and IMARPE data, except in late winter-early spring where modeled Chl was close to IMARPE.

### 3.1.2. Interannual Variability
### 3.1.2.1. Vertical Structures
Alongshore-averaged vertical sections of temperature, Chl, and nitrate for the model and IMARPE data are shown for neutral and EN periods in Figure 3. Near-surface slanted isotherms (for the model and observations) were present during neutral and EN event, indicating the occurrence of coastal upwelling (Figures 3a,
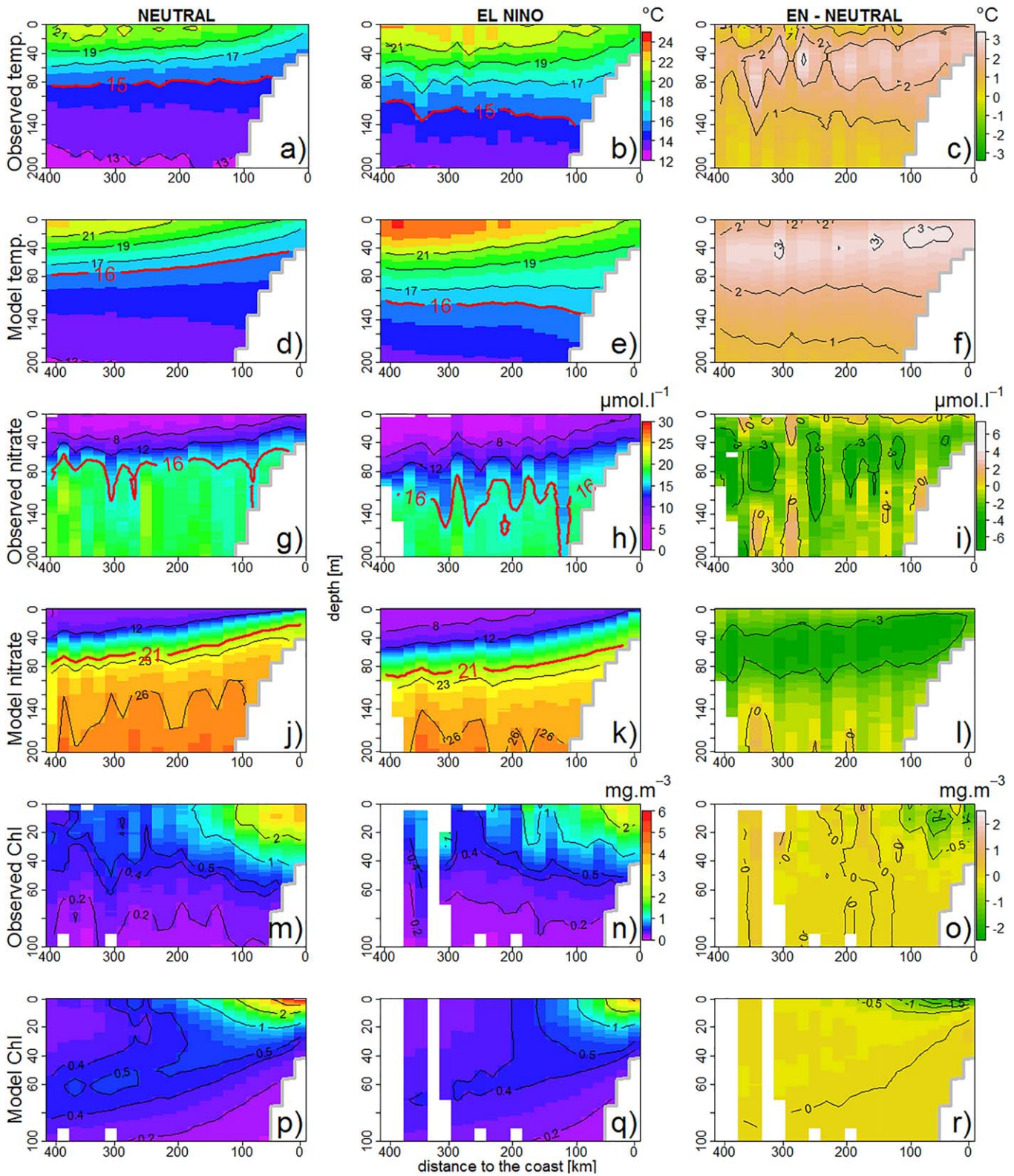
**Figure 3.** Along-shore averaged vertical section (between 6°S and 16°S) of observational data from IMARPE and model variables: (a–f) temperature (°C), (g–l) nitrate (μmol.L$^{-1}$), and (m–r) chlorophyll (mg.m$^{-3}$). (left column) Neutral periods, (middle column) El Niño periods, and (right column) differences between EN and Neutral period are shown. Red lines mark ZT (Figures 3a, 3b, 3d, 3e) and ZNO$_3$ (Figures 3g, 3h, 3j, 3k).

3b, 3d, and 3e). During neutral periods, between the coast and 200 km offshore, ZT was found at ∼80 m depth for IMARPE (Figure 3a) and ∼60 m depth in the model (Figure 3d). In contrast, during EN periods ZT deepened up to ∼130 m depth for IMARPE (Figure 3b) and the simulation (Figure 3e). Despite a slight warm bias, the simulation clearly reproduced the higher temperature anomalies in the surface layer (> +2°C) above 80 m depth (Figures 3c and 3f) and the ZT deepening during EN.

The nitrate vertical sections indicated a model positive bias (∼6–8 $\mu mol.L^{-1}$) below the surface layer (located below the 17°C and 19°C isotherms during neutral and EN periods, respectively) (Figures 3g, 3h, 3j, and 3k). During neutral periods and between the shelf and 200 km, $ZNO_3$ was localized between ∼60 m and 80 m depth for IMARPE (Figure 3g) and between ∼30 m and 60 m depth in the model (Figure 3j). During EN, both the model and IMARPE data showed a deepening of $ZNO_3$. $ZNO_3$ was highly variable in the observations (Figures 3g and 3h) but its mean depth (between the shelf and 200 km) during EN was ∼120 m depth for IMARPE (Figure 3h) and ∼70 m depth for the model (Figure 3k). Negative anomalies (< −3 $\mu mol.L^{-1}$) indicated substantial nitrate loss in both the model (between 5 and 90 m depth) and the observations (between 30 and 125 m depth) (Figures 3i and 3l).

The Chl vertical sections presented high values in the nearshore surface layer, in the model and observations (Figures 3m–3q). During neutral periods the 2 $mg.m^{-3}$ isoline reached the surface 100 km offshore both in IMARPE data (Figure 3m) and the simulation (Figure 3p). Within the first 50 km nearshore, surface mean values were ∼3.5 $mg.m^{-3}$ for IMARPE data and ∼4.5 $mg.m^{-3}$ for the simulation. Note also the thicker highly productive layer (>2 $mg.m^{-3}$) in the observations (Figure 3m). The remotely sensed decrease of surface Chl concentration evidenced during EN [e.g., *Carr et al.*, 2002] was also found in IMARPE data and the model (Figures 3n and 3q). Within 100 km from the coast, in the surface layer (<10 m depth), a chlorophyll decrease was found in the observations (∼ −0.7 $mg.m^{-3}$) and the model (∼ −1.5 $mg.m^{-3}$). However, the observations showed a deeper Chl decrease: the −0.5 $mg.m^{-3}$ isoline reached ∼35 m depth in IMARPE data and ∼15 m depth in model (Figures 3o and 3r).

### 3.1.2.2. Interannual Time Series

Interannual variations of the model physical (SSH, SST, and ZT) and biogeochemical ($ZNO_3$ and surface Chl) variables were evaluated in the coastal region (see Figure 1 and section 2.5). Five day average modeled SSH
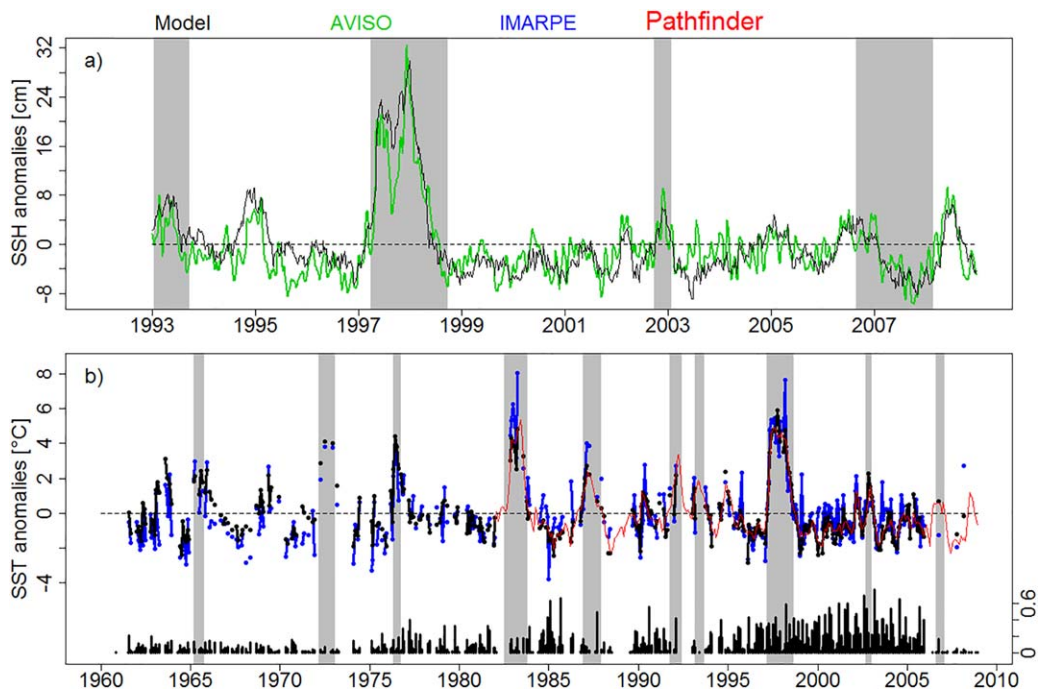


**Figure 4.** (a) Time series of sea level anomaly (5 day averages, in cm) from AVISO (green line), and model (black line) and (b) monthly SST anomalies (°C) from IMARPE (blue line), model (black line), and Pathfinder data (red line). The averages were computed in a coastal box (see Figure 1). Monthly coverage ratio (see section 2.5) in the coastal box (bottom black bars) is also shown in Figure 7c. Shaded grey boxes represent El Niño periods.

anomalies reproduced well the sea level variability during the four EN events from 1993 to 2008 (Figure 4a), in particular the two peaks associated with the passage of CTW trains during the 1997–1998 event [*Colas et al.*, 2008]. The SSH time series anomalies had a correlation coefficient of 0.86.

The model reproduced well the SST variability in particular the SST increase during EN (Figure 4b). Monthly SST anomalies had a high correlation with IMARPE data (~0.8) and with Pathfinder (~0.9). During the 1982–1983 and 1997–1998 events, respectively, mean maximum SST anomalies of ~ +2.9°C and ~ +3.2°C were simulated, weaker than IMARPE anomalies (~ +4.2°C, ~ +3.4°C) but very similar to Pathfinder anomalies (~+2.5°C, ~ +3.2°C). The ISR(SST) presented low values (~2%) indicative of robust estimates (Figure 6a).

Figure 5 shows the interannual variations of ZT, $ZNO_3$, and surface Chl concentration over 1958–2008. The simulation reproduced the deepening of the thermocline during most EN events (Figure 5a). On average, ZT was found at ~55 m depth in both the observations and the simulation. During the 1997–1998 EN (the best sampled event in terms of temperature), the observed ZT depth was ~120 m and ~140 m in the model. Correlation between modeled and observed ZT is 0.7. Mean ISR(ZT) was ~23% during the studied period (Figure 6b).

The interannual variations of the $ZNO_3$ are displayed in Figure 5b. Modeled $ZNO_3$ was slightly shallower (~36 m depth) than the observed (~45 m depth) during study period. The model simulated a strong deepening event during the 1982–1983 (~ +23 m) and 1997–1998 (~ +30 m) events, also found in the observations (~ +25 m in both events). However, modeled and observed $ZNO_3$ time series were poorly correlated (~0.3) over the entire time period. Mean ISR($ZNO_3$) was ~25% (Figure 6c).

Relatively low Chl concentrations were observed during the 1982–1983 (~1.8 mg.m$^{-3}$) and 1997–1998 (~1.7 mg.m$^{-3}$) events, with respect to time periods preceding and following the events, which was
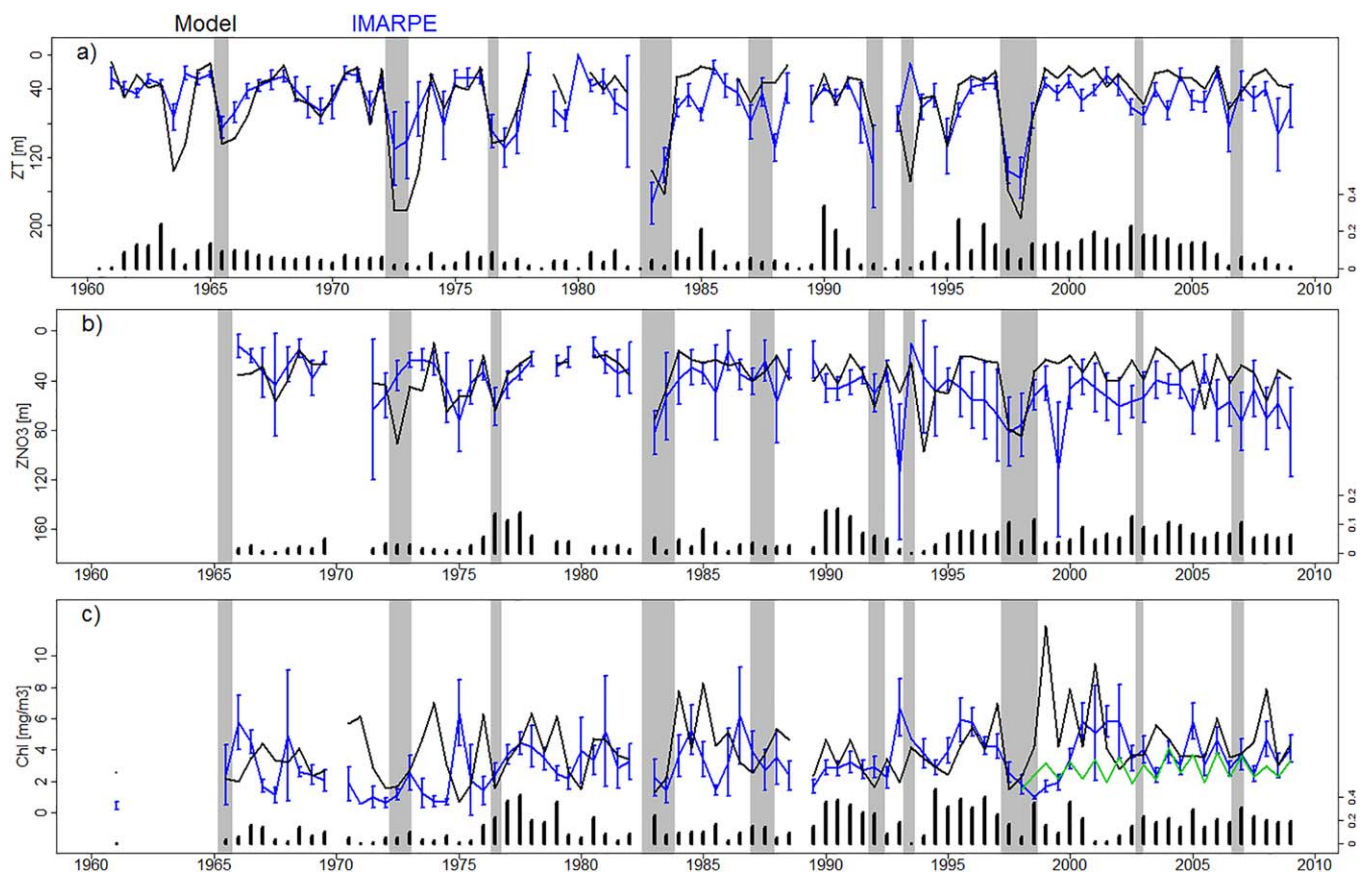


**Figure 5.** Time series of (a) ZT (in meters), (b) $ZNO_3$ (in meters), and (c) surface chlorophyll (in mg.m$^{-3}$). Data were averaged each semester for IMARPE (blue line) and model (black line) and SeaWIFS (green line). Error bars represent standard deviation for IMARPE data. Beside, coverage ratio (bottom black bars) is presented. The model mean was computed using the IMARPE sampling (gaps meaning not data), and for SeaWIFS all available data were used.
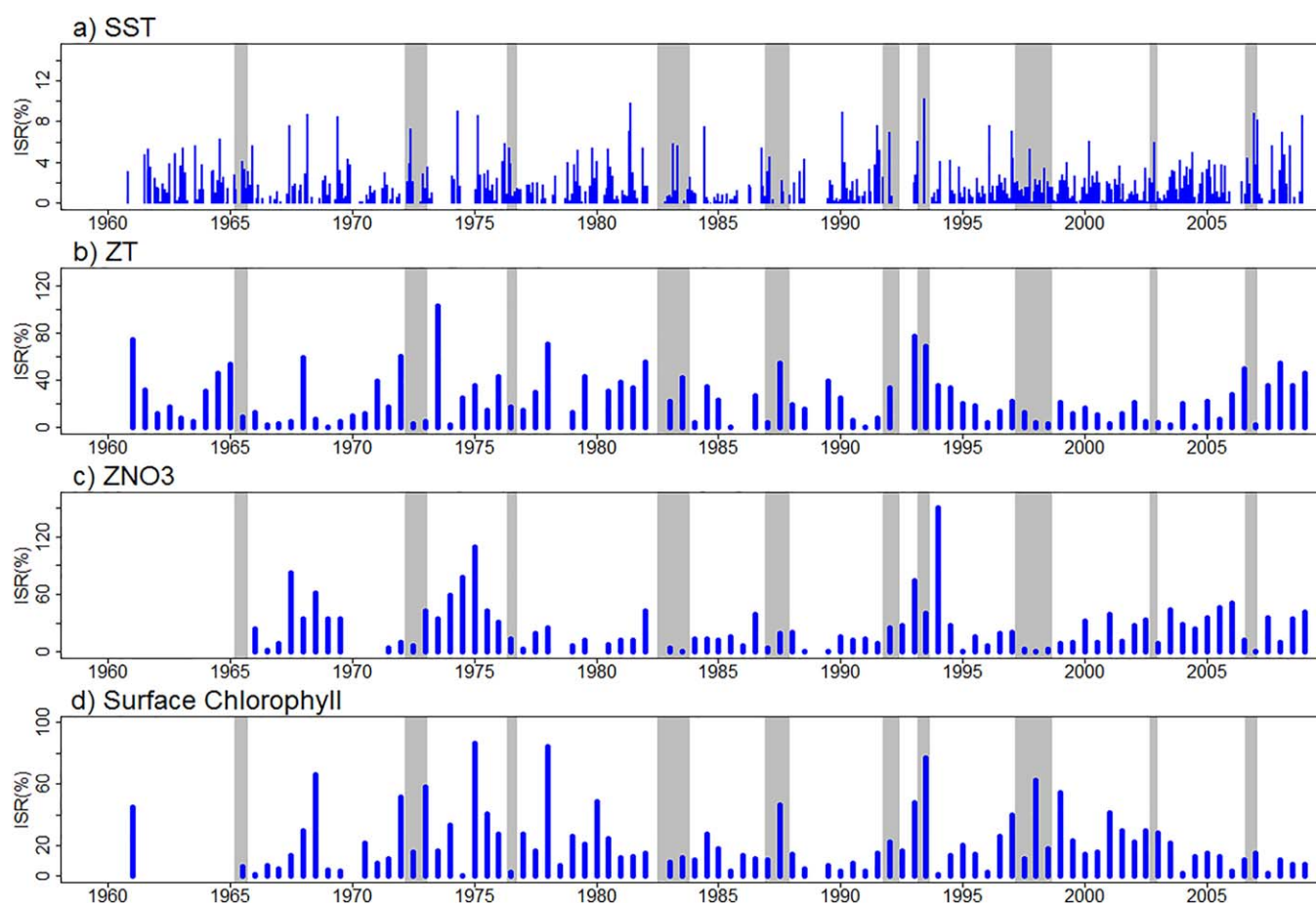
**Figure 6.** ISR (in %) for (a) SST, (b) ZT, (c) ZNO$_3$, and (d) Chl. Monthly and 6-month averages are shown in Figures 6a and 6b–6d, respectively. ISR was computed in a coastal band (see Figure 1). Shaded grey boxes represent El Niño events.

reproduced by the simulation. However, there was no correlation between the model and IMARPE observations. The Chl concentration averaged over all EN periods was lower ($\sim$2.5 mg.m$^{-3}$ for both model and data) than the mean over the full time period ($\sim$4 mg.m$^{-3}$ for the model and $\sim$3.2 mg.m$^{-3}$ for the data). Model and SeaWIFS data confirmed that negative Chl concentration anomalies were found during EN 1997–1998 (supporting information Figure S1b). However a weak interannual variability was evidenced in SeaWIFS in comparison with in situ data. Note that SeaWIFS Chl concentration mean is affected by the presence of important cloud coverage [*Wood et al.*, 2011; *Echevin et al.*, 2014]. ISR was $\sim$18% during neutral periods and EN events (Figure 6d). However high ISR values in some years (e.g., 60% in the first semester of 1998) suggest that some of the discrepancies between model and data may be attributed to insufficient observational sampling.

### 3.2. Impact of EN in Phytoplankton Groups

Both diatoms and nanophytoplankton, the two phytoplanctonic groups represented by the model, displayed negative Chl anomalies during EN events. EN events impacted in different proportion the two phytoplankton groups: the Chl loss represented $\sim -50\%$ for diatoms (particularly in late spring-summer) and $\sim -20\%$ for nanophytoplankton. The lowest Chl values were found during the 1972–1973, 1982–1983, and 1997–1998 events, with values of $\sim -4$ mg.m$^{-3}$ for diatoms and $\sim -0.15$ mg.m$^{-3}$ for nanophytoplankton (Figure 7a). EN events also had a different impact on their seasonal cycles. The seasonal cycle of nanophytoplankton during neutral periods presented relatively weak peaks during early autumn and late spring ($\sim$0.6 mg.m$^{-3}$) and low values during late spring-summer ($\sim$0.39 mg.m$^{-3}$) and barely changed during EN (Figure 7b). Diatoms, the dominant species in the Peru upwelling system [*Sánchez*, 2000], were much more impacted, as they are less adapted to nutrient-poor waters [*Irwin et al.*, 2006]. The late spring-early
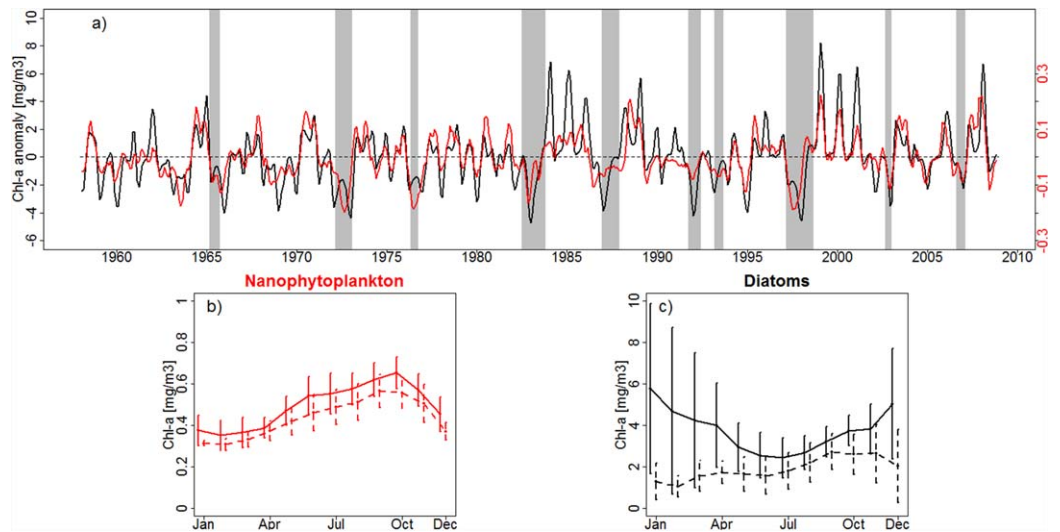
**Figure 7.** (a) Time series of model nanophytoplankton (red line) and diatoms (black line) surface chlorophyll concentration (in mg.m$^{-3}$) anomalies. Anomalies were low-pass filtered. Note the different vertical scales for the two time series. Seasonal cycle of (b) nanophytoplankton and (c) diatoms surface chlorophyll concentration (in mg.m$^{-3}$) during composite El Niño (dashed line) and Neutral (thick line) periods. Error bars represent standard deviation.

summer peak ($\sim 5$ mg.m$^{-3}$) disappeared completely ($\sim 1.5$ mg.m$^{-3}$) and a peak was found in late winter-beginning spring ($\sim 2.5$ mg.m$^{-3}$) during EN events. The Chl in diatoms decrease reached $\sim -60\%$ during summer and $\sim -25\%$ during winter (Figure 7c).

### 3.3. Processes Driving the Chlorophyll Decrease During EN
### 3.3.1. Poleward Propagation of CTW

Figure 8 displays the alongshore signature of the poleward propagating CTW on SSH, ZT, ZNO$_3$, and surface Chl particularly during the two strong EN events (1982–1983 and 1997–1998) simulated by the model. The slanted isolines in each panel indicate southward propagation. Three downwelling EKW in 1982–1983
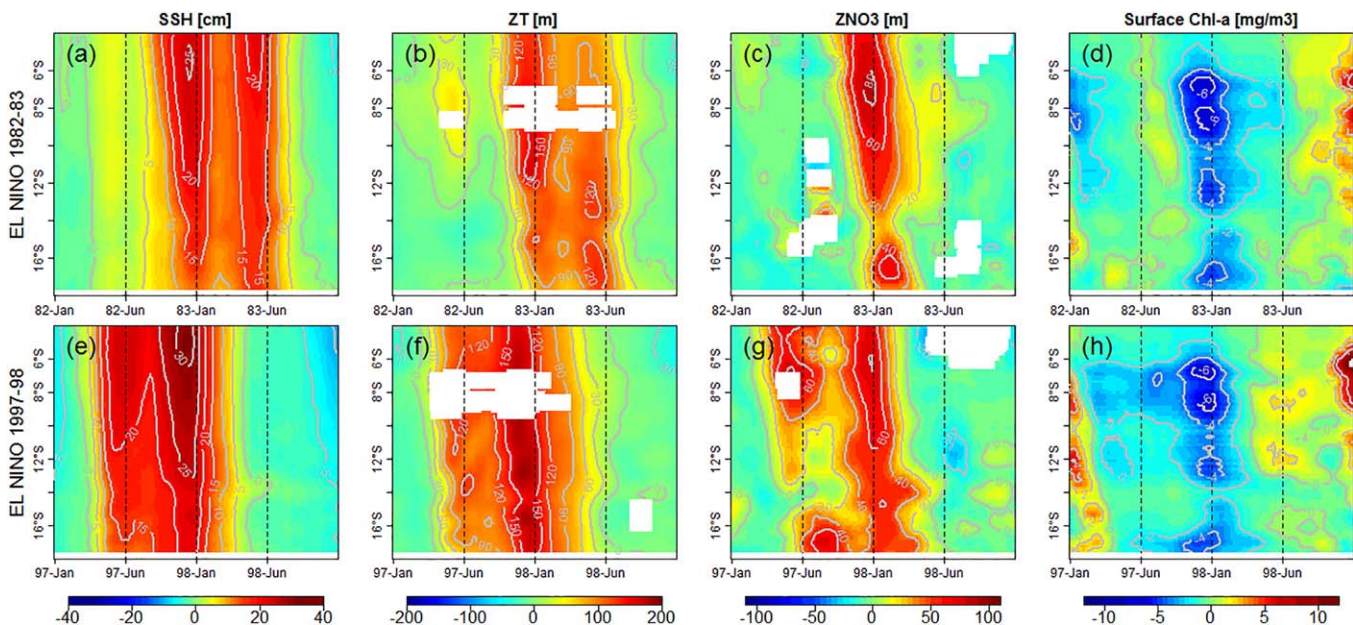


**Figure 8.** Hovmoller (latitude versus time) of (a, e) model sea level (in cm), (b, f) ZT (in meters), (c, g) ZNO$_3$ (in meters), and (d, h) surface chlorophyll (in mg.m$^{-3}$) anomalies during the (top) 1982–1983 and (bottom) 1997–1998 El Niño events. Model values were averaged between the coast and 100 km. All variables were filtered in time (60 days moving average) and space (100 km alongshore). Missing data in Figures 8b, 8c, 8f, and 8g indicate that ZT and ZNO$_3$ were not detected from 100 km to the coast because of their deepening during EN.

(respectively, two in 1997–1998) propagated eastward (supporting information Figure S2) and triggered downwelling CTW upon reaching the Ecuadorian coasts. During both EN events, a more intense CTW is seen during spring-early summer, as well as a weaker CTW in autumn of 1983 and late autumn-early winter of 1997. The passage of the downwelling CTW generated a SSH rise, with maximum values around ∼25 cm and ∼35 cm during the peak of the strongest CTW for the 1982–1983 and 1997–1998 events, respectively (Figures 8a and 8e). The amplitude of SSH anomalies decreased by ∼40–50% between 4°S and 18°S, as the CTW energy dissipated during its poleward propagation.

In association with the sea level rise, ZT deepened during the passage of the CTWs. Anomalies peaked at ∼110 m and ∼160 m in late spring-early summer 1982–1983 and 1997–1998, respectively (Figures 8band 8f). The nutricline depth was also affected: during the 1982–1983 EN $ZNO_3$ deepening (∼50 m, Figure 8c) was observed in late spring-summer, whereas during 1997–1998 the nutricline deepened during two successive periods, first in autumn-early winter 1997 and then in late spring-summer 1998. The spring-summer CTW had the largest impact (∼55 m; Figures 8c and 8g).

The CTW generated strongly negative surface Chl anomalies. Expectedly, the CTW impact was stronger during late spring-summer ($\sim -4.5$ mg.m$^{-3}$) than during autumn ($\sim -2$ mg.m$^{-3}$), due to the higher Chl concentration and greater deepening of the nutricline/thermocline in summer. This increased both nutrient limitation of phytoplankton growth during EN, but light limitation was also increased due to a deepening of the mixed layer during EN (see section 4.2 and supporting information Figure S3). The latitude band between 6°S and 9°S (e.g., the northern shelf region) was mostly affected (anomalies less than −6 mg.m$^{-3}$; Figures 8d and 8h) due to the higher modeled Chl values in this region.

### 3.3.2. Nearshore Vertical Fluxes

During neutral periods the wind stress had a marked seasonality, with a maximum during late winter (∼5.5 10$^{-2}$ N.m$^{-2}$) and low values during summer (∼1.7 10$^{-2}$ N.m$^{-2}$) in the simulation (Figure 9a) and in observations [Gutiérrez et al., 2011]. The wind stress was roughly in phase with the seasonal cycle of mass vertical
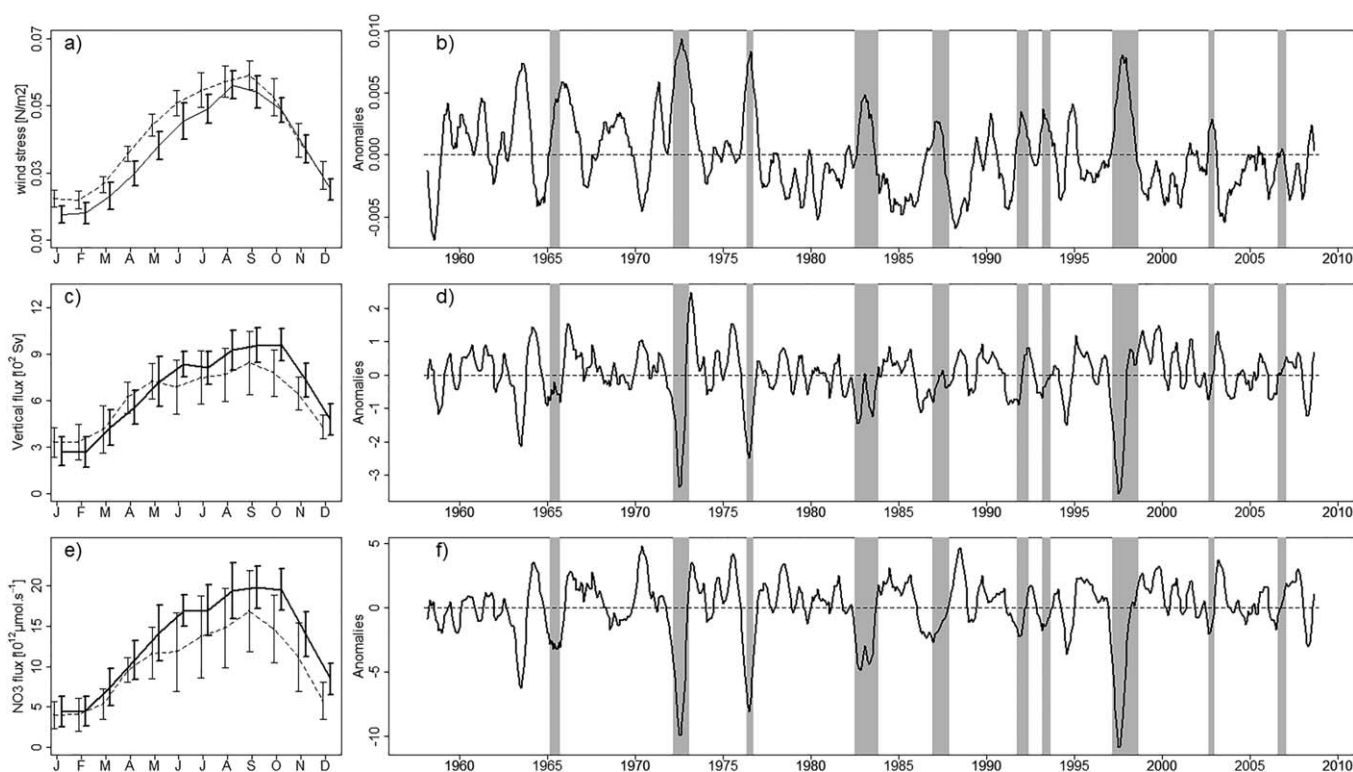


**Figure 9.** (a, c, e) Seasonal cycle and (b, d, f) interannual time series of low-pass filtered anomalies for (a and b) wind stress (N.m$^{-2}$), (c and d) mass vertical flux (in Sv) at 20 m depth, and (e and f) nitrate vertical advection flux at 20 m depth (in μmol.s$^{-1}$) during Neutral (thick line) and EN periods (dashed line). All model variables were averaged in a coastal band (see Figure 1).

flux (referred to as the upwelling) and nitrate vertical flux (Figures 9b and 9c). The vertical fluxes were also modulated by seasonal CTW which had different amplitude and timing, as shown in *Echevin et al*. [2011].

During EN, alongshore winds increased off Peru [*Enfield*, 1981; *Kessler*, 2006]. The mean wind stress anomalies were around $\sim$0.35 $10^{-2}$ N.m$^{-2}$ (Figure 9b) with stronger anomalies in summer-autumn (Figure 9a). The strongest anomalies were found during the 1972–1973 and 1997–1998 EN events with $\sim +0.7\ 10^{-2}$ N.m$^{-2}$. Other EN events presented a $\sim +0.25\ 10^{-2}$ N.m$^{-2}$ anomaly on average. The wind stress increase during EN generated a mixed layer deepening (supporting information Figure S3).

These wind stress positives anomalies suggest that the wind-driven upwelling could be enhanced during EN events. However, the model showed an upwelling decrease during winter-spring (Figure 9c), which was associated to a compensating onshore current during EN (Figure 1 and see section 4.3). The mean upwelling anomalies were $\sim -0.6\ 10^{2}$ Sv and the highest negative anomalies were encountered during the 1972–1973 and 1997–1998 events ($\sim -3.2\ 10^{2}$ Sv; Figure 9d). Expectedly, the nitrate flux decreased during EN due to both a nearshore reduction of the vertical velocity and a deepening of the nutricline, particularly in winter-spring, while summer was less impacted (Figure 9e). The maximum negative anomalies occurred during the 1997–1998 event. The mean modeled nitrate flux anomalies were around $\sim -3.4\ 10^{12}$ µmol.s$^{-1}$ during EN events (Figure 9f).

### 3.3.3. Modification of the Source Water Properties

Using the virtual floats released in the upwelling region and integrated backward in time, we computed histograms of the source water (SW) depth and nitrate concentration for neutral and EN composite years.

The mean depth of the SW, 1 month before being upwelled, had a marked seasonal pattern (Figure 10a). During austral summer, water parcels were located within the upper 120 m of the water column, with a maximum probability ($\sim$70%) between 25 and 40 m depth. During austral winter the parcels depth spanned a wider depth-range (between the surface and 180 m), and 40% of the upwelled water came from the 60–100 m
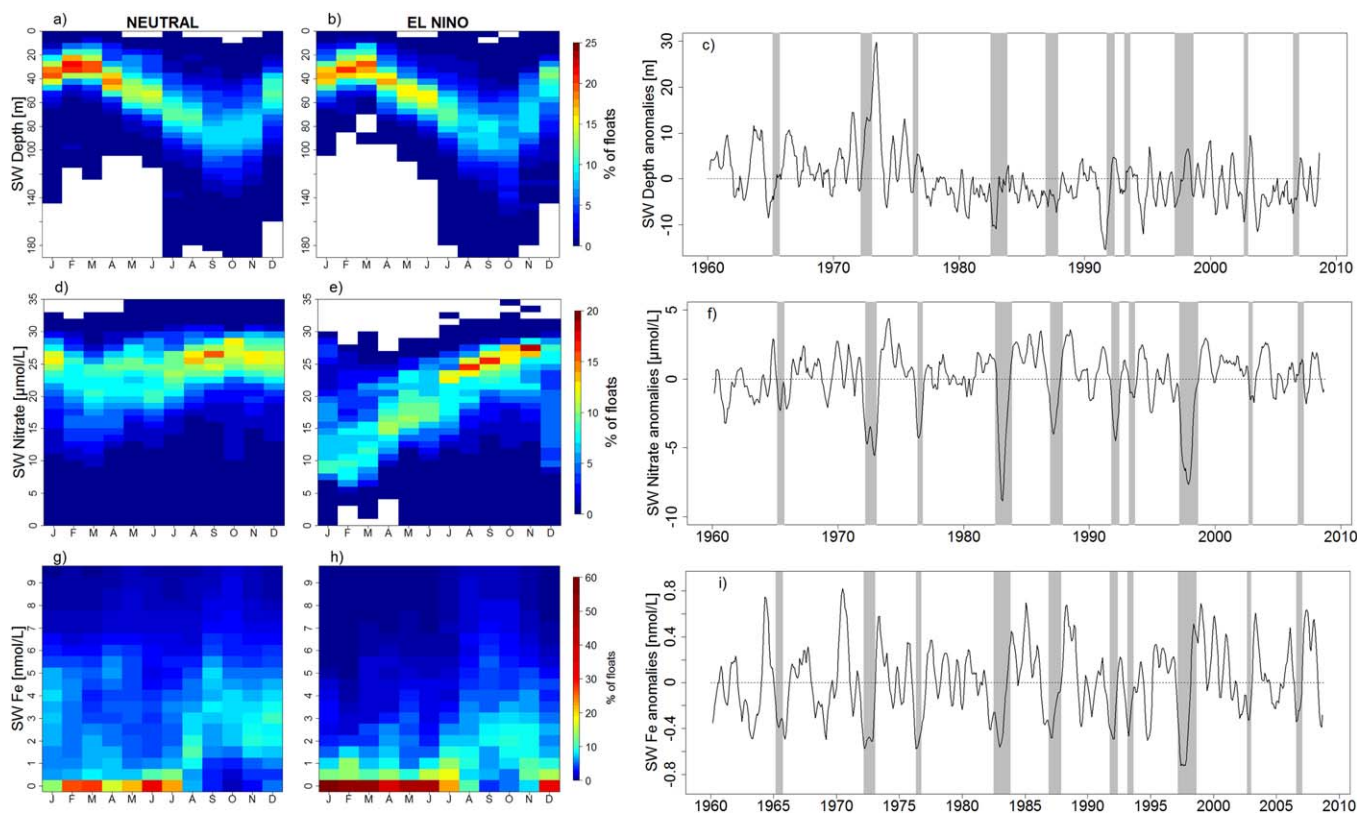


**Figure 10.** (a and b) Seasonal variation of source water depth (in meters), (d and e) nitrate concentration (in µmol.L$^{-1}$), and (g and h) iron concentration (in nmol.L$^{-1}$) 1 month before their upwelling at the coast. Histograms are presented for (left column) Neutral and (right column) El Niño periods. The color scale indicates the percentage of floats in each bin. Time series of (c) SW depth (in meters), (f) nitrate concentration (in µmol.L$^{-1}$), and (i) iron concentration (in nmol.L$^{-1}$) anomalies. Times series were low-pass filtered using 6 month moving average filter.

depth range. Interestingly, during EN, the SW depth was little modified (Figure 10b): it had the same seasonality, with a slightly narrower vertical range (between 0 and 80 m depth) in summer, likely due to an enhanced stratification caused by the shoreward advection of anomalously warm waters [Colas et al., 2008].

During neutral years, the SW nitrate concentration showed a weak seasonality with a slightly higher concentration ($\sim$22–30 $\mu$mol.L$^{-1}$) during winter-early summer than during late summer-autumn ($\sim$17–25 $\mu$mol.L$^{-1}$; Figure 10d). During EN events, the percentage of SW parcels with a high concentration of nitrate dropped dramatically in summer and autumn. A large portion ($\sim$40%) had concentrations between $\sim$7 and 12 $\mu$mol.L$^{-1}$ in summer and $\sim$12 and 17 $\mu$mol.L$^{-1}$ in autumn, which represented a 40% decrease. During winter and spring, the SW nitrate content was not significantly altered (Figure 10e). Expectedly, the time series of SW depth anomalies did not exhibit a clear behavior during EN events (Figure 10c). In contrast, the strongest nitrate anomalies were found during the 1972–1973, 1982–1983, and 1997–1998 events with peaks of $-5.5$ $\mu$mol.L$^{-1}$, $-9$ $\mu$mol.L$^{-1}$, and $-8$ $\mu$mol.L$^{-1}$, respectively (Figure 10f).

SW iron (Fe) concentration was also evaluated. The role of iron limitation during EN has been little investigated, however its impact on phytoplankton growth off Peru has been documented [Hutchins et al., 2002; Bruland et al. 2005]. Our Lagrangian analysis showed that the SW Fe concentration strongly decreased during EN (Figure 10i), especially during summer – autumn, where $\sim$70% of floats presented concentrations less than 0.5 nmol.L$^{-1}$ (Figures 10g and 10h). During the peak of EN (e.g., January 1998), surface Fe positive anomalies were found offshore (>40 km; Figure not shown). It is likely that the low phytoplankton biomass did not consume the upwelled Fe which accumulated and was transported offshore by Ekman currents. However, to our knowledge there was no available Fe data collected during EN to confirm this mechanism.

In a second experiment (see section 2.2), we focused on the changes in SW characteristics away from the upwelling region, e.g., in the equatorial zone when SW crossed the longitude 88°W. In this experiment, more than 95% of the floats were found between 2°N and 10°S. In Figure 11 we displayed some properties of the floats at 88°W: the time to reach the upwelling region, depth, and nitrate concentration. We also contrasted LN, neutral, moderate, and extreme EN events. During extreme events, water particles reached the coastal zone more rapidly ($\sim$6 months) than in neutral conditions ($\sim$10 months), and floats during LN periods transited in an even longer time ($\sim$14 months; Figure 11a) in line with Montes et al. [2011]. In addition, during extreme EN events floats were shallower ($\sim$90 m) than during neutral and moderate events ($\sim$105 m). Floats were much deeper ($\sim$155 m) during LN (Figure 11b).

The SW nitrate content at 88°W were depleted only during extreme EN events. In such conditions, particles carried at least 20% less nitrate ($\sim$20 $\mu$mol.L$^{-1}$) than during LN, neutral and EN moderate. Besides, SW nutrient concentration during LN was not very different than during neutral and EN periods (Figure 11c).

### 3.3.4. Enhanced Mesoscale Turbulence

The EKE increased during EN, particularly during extreme events (1972–1973, 1982–1983, 1997–1998). The amplitude of the modeled EKE increase during the 1997–1998 EN was consistent with the observations (Figure 12a). Chaigneau et al. [2008] also found a 40% increase in satellite-derived eddy activity during the 1997–1998 event. We evaluated the nitrate flux in the offshore region. In Figure 12b the mean vertical flux
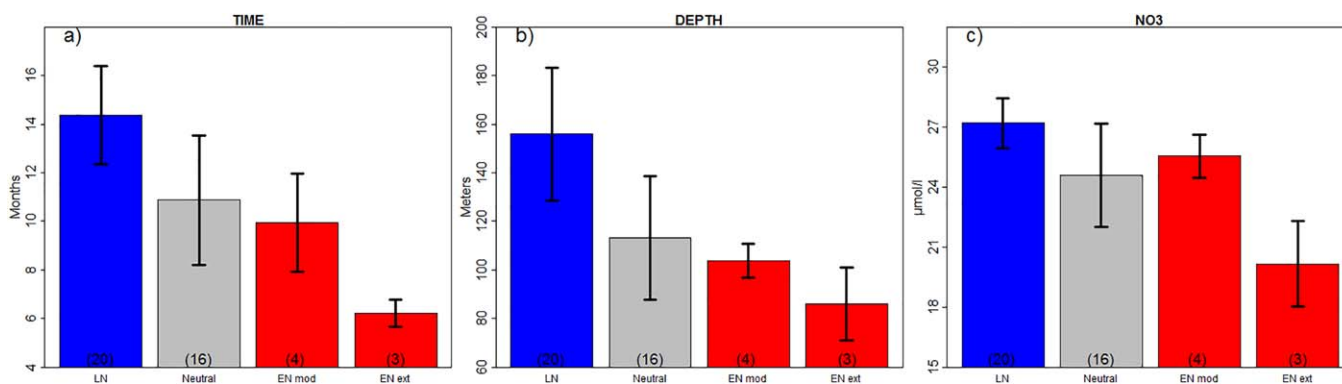


**Figure 11.** (a) Transit time (from 88°W to the coast) (in months), (b) depth (in meters), (c) nitrate concentration (in $\mu$mol.L$^{-1}$), and (d) iron concentration (in nmol.L$^{-1}$) of equatorial source waters (at 88°W) during LN events (blue bars), Neutral periods (grey bars), EN moderate and EN extreme events (red bars). Error bars represent standard deviation. Numbers at the bottom of the bars indicate the number of events taken into account to compute the average. Floats were released between October and December.
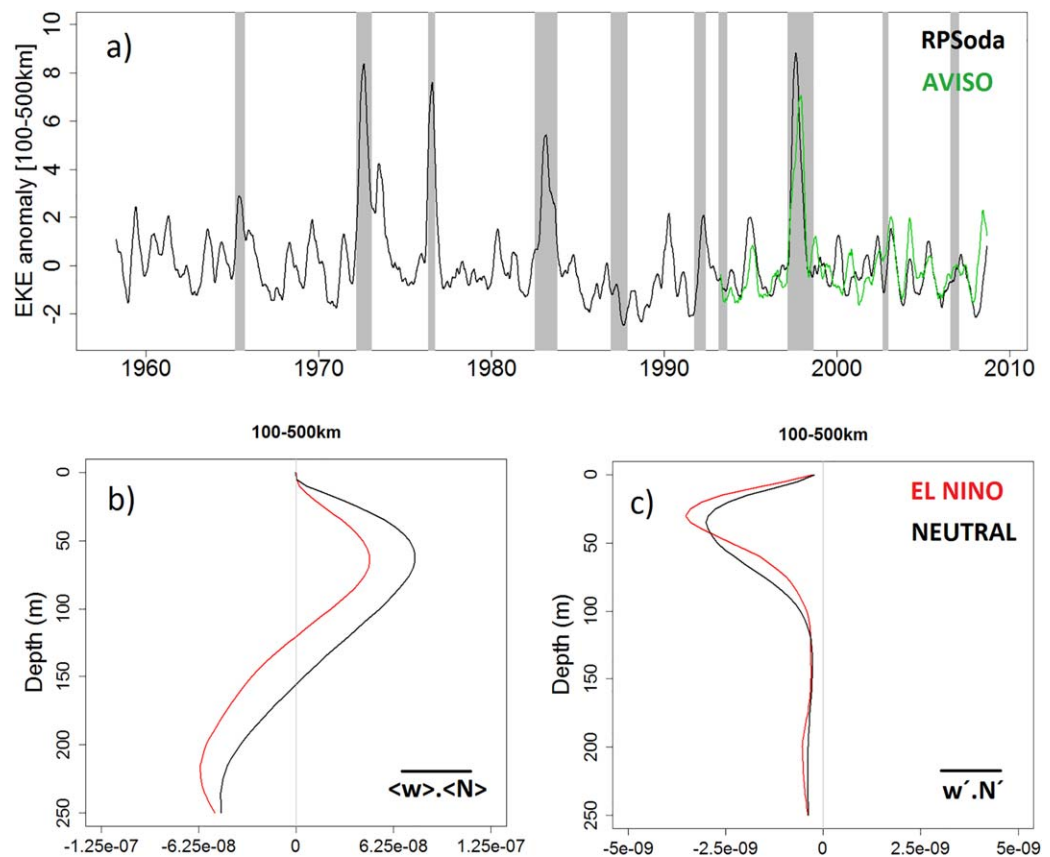
**Figure 12.** Times series of geostrophic Eddy Kinetic Energy (EKE, in $cm^2.s^{-2}$) anomaly in an offshore oceanic band (100–500 km from the coast and 6°S–14°S). Geostrophic currents anomalies were computed with respect to a 60 days moving average filter for model (black line) and AVISO data (green line). (a) The EKE times series was low-pass filtered using a 6 month moving average filter. (b) Vertical profile of mean vertical nitrate flux (in $\mu mol.m^{-2}.s^{-1}$) and (c) eddy vertical nitrate flux (in $\mu mol.m^{-2}.s^{-1}$) for Neutral (black line) and EN periods (red line). The nitrate fluxes were computed in an oceanic band between 100 and 500 km from the coast and 6°S–14°S.

($\overline{\langle w \rangle . \langle N \rangle}$) showed positive values between ~5 and ~130 m depth, likely related to Ekman pumping [e.g., *Albert et al.*, 2010]. During EN, the mean flux decreased due to a reduced Ekman pumping [*Halpern*, 2002] and lower nutrient concentration. In contrast, the nitrate eddy flux presented negative values with a maximum at ~40 m depth during neutral ($-3 \; 10^{-9}$ $\mu mol.m^{-2}.s^{-1}$) and EN ($-3.5 \; 10^{-9}$ $\mu mol.m^{-2}.s^{-1}$) years (Figure 12c). This eddy-driven subduction (or nitrate vertical eddy flux) represents a fraction of the mean vertical flux ($\overline{w'.N'} / \overline{\langle w \rangle . \langle N \rangle}$): ~6% and ~12% (between 30 and 70 m) for neutral and EN periods, respectively.

### 3.4. Impact of EN Intensity and LN Conditions

In this section we characterized the impact of different EN intensities (moderate and extreme) and the impact of LN on modeled wind stress, upwelling, ZT, $ZNO_3$, Chl, and SW properties in the coastal region (Figure 13). Expectedly, extreme EN events had the strongest impact on wind stress increase, upwelling decrease, ZT and $ZNO_3$ deepening, SW nitrate and iron concentration, and surface Chl. The SW depth (one month before upwelling) were unchanged regardless of the event intensity. Interestingly, during LN the coastal system tended to be slightly more productive than during neutral periods, due to an enhanced upwelling (Figure 13b) and slightly nutrient-richer SW (Figures 13f and 13g).

In general EN impacts on physical and biogeochemical variables (negative or positive anomalies) were about twice as strong as LN impact and of opposite sign. However a fully dedicated study would be necessary to investigate further the processes at play during LN events.

### 3.5. Impacts of EN on Zooplankton and Carbon Export

EN impacted the higher trophic levels of the ecosystem [*Ñiquen and Bouchón*, 2004], as for instance the modeled zooplankton stocks (Figures 14a and 14b). Both mesozooplankton and macrozooplankton showed
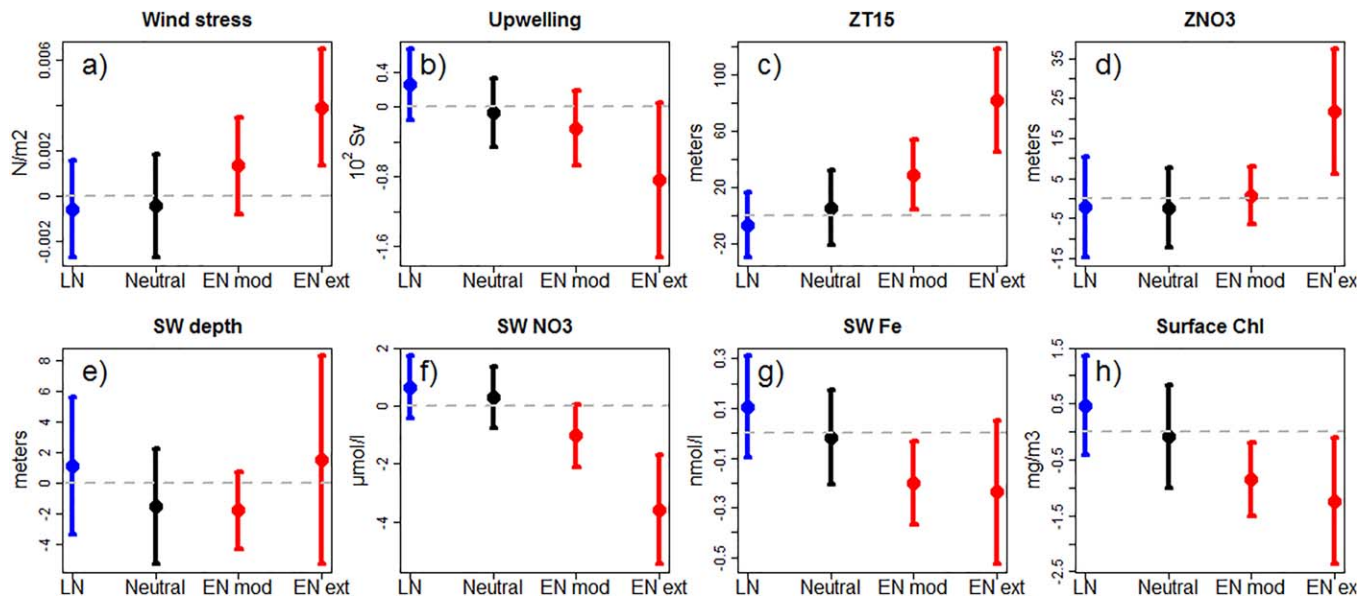
**Figure 13.** (a) Wind stress (in N.m$^{-2}$), (b) upwelling rate (in $10^2$ Sv), (c) ZT (in meters), (d) ZNO$_3$ (in meters), (e) SW depth (in meters), (f) SW nitrate concentration (in $\mu$mol.L$^{-1}$), (g) SW iron concentration (in nmol.L$^{-1}$), and (h) Chl concentration (in mg.m$^{-3}$) during LN (blue bar), Neutral (black bar), EN moderate and EN extremes (red bars). All variables are averaged in a coastal band (see Figure 1). Error bars represent the standard deviation.

strongly negative anomalies during EN, reaching 35–40% during extreme events. Nevertheless, observational data in Peru did not show a clear relationship between EN events and a decrease of zooplankton biomass. The observed interannual variability seems dominated by decadal regime shifts [*Ayon et al.*, 2008a] and is supposed to be partly controlled by fish predation at the local scale [*Ayon et al.*, 2008b]. Note that zooplankton predation by higher trophic levels is crudely parameterized in PISCES (see section 2.1.1 and *Aumont et al.*, [2015]). South of the Peru region, off central Chile, a systematic decrease of zooplankton during EN was not observed, as specific types of zooplankton can thrive during EN conditions [*Ulloa et al.*, 2001]. Possibly, the coupling of our model with a higher trophic level model [e.g., *Travers et al.*, 2009; *Hernandez et al.*,2014; *Lefort et al.*, 2015] could help disentangle the bottom-up and top-down mechanisms that control the zooplankton biomass during EN. Besides, export and remineralization of organic matter
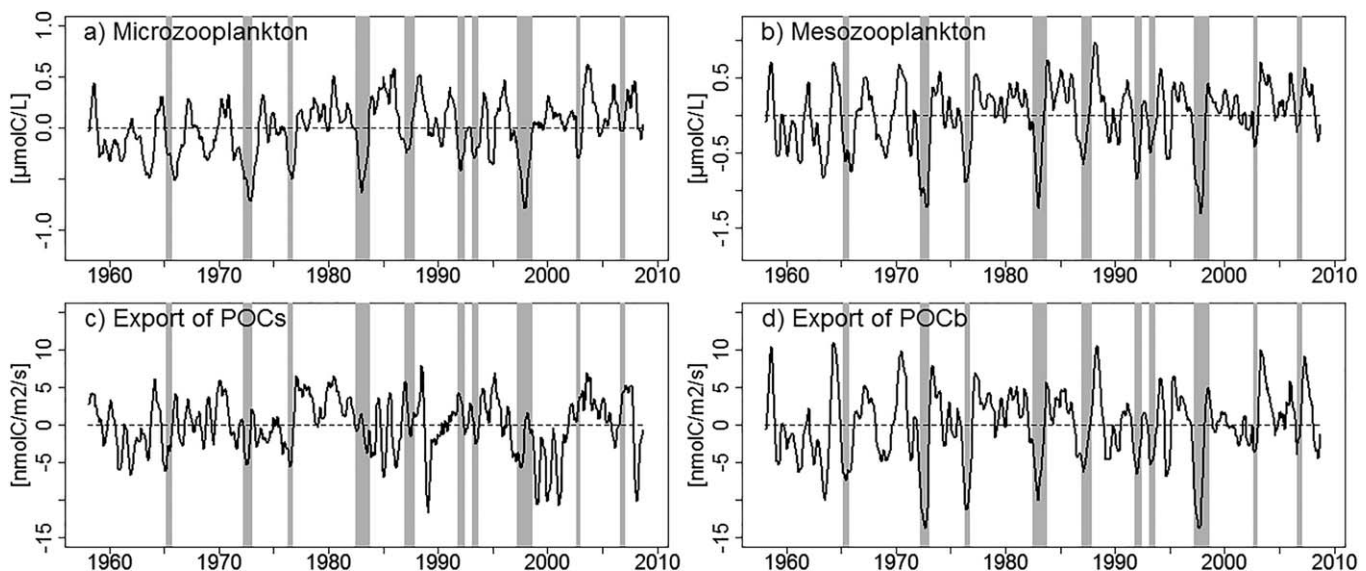


**Figure 14.** Time series of modelled zooplankton surface concentration (in $\mu$molC.L$^{-1}$): (a) microzooplankton and (b) mesozooplankton, (c) small and (d) big POC downward flux (in nmolC.m$^{-2}$.s$^{-1}$) anomalies. All variables were averaged in a coastal band (see Figure 1) and filtered using a s6 month moving average filter.

play an important role in the maintenance of the Peru OMZ [*Paulmier et al.*, 2006; *Graco et al.*, 2007]. The simulated export of organic matter, namely through sedimentation of particulate organic carbon (POC) in the form of big (POCb, 100–5000 $\mu$m) settling particles, was strongly reduced during EN (Figures 14c and 14d), while the small POC export (POCs, 1–100 $\mu$m) did not have a clear relationship with EN events. The average anomaly of POCb export was $\sim$–4.5 nmolC.m$^{-2}$.s$^{-1}$ during EN, and reached $\sim$–10 nmolC.m$^{-2}$.s$^{-1}$ ($\sim$50% loss) during strong events (e.g., 1997–1998). A strong export decrease was also found by *Carr* [2003] during the 1997–1998 event with minimums values during the passage of CTW.

## 4. Discussion

### 4.1. Model-Data Discrepancies

Rather expectedly, the model reproduced more accurately the physical variability than the biogeochemical variability observed from IMARPE surveys. Surface Chl and nutrients have a high variability in space and time due to nonlinear biogeochemical processes involved in primary productivity. Daily variability can reach 1 order of magnitude, e.g., in the case of fast blooms associated with red tides [*Kahru et al.*, 2004]. Also, strong horizontal gradients due to mesoscale and submesoscale features [*Chaigneau et al.*, 2008; *Colas et al.*, 2013; *McWilliams*, 2016] are commonly observed and not well represented in our model because of its relatively low spatial resolution (1/6°).

Estimation of a coastal index for the entire Peru region based on IMARPE in situ data (e.g., Figure 3) could also be partly biased due to the cruises sampling. Low values of ISR for some variables suggest that IMARPE in situ sampling was able to represent the oceanographic conditions along the coasts. Relatively good spatial sampling of SST in situ measurements resulted in low values of ISR ($\sim$3%) and hence good representativity (Figure 6a). In contrast, the highly heterogeneous surface Chl produced a higher ISR ($\sim$20%, Figure 6d) in spite of a relatively large number of samples. High ISR values ($\sim$20%) for the thermocline and nutricline (Figures 6b and 6c) were likely due less numerous subsurface measurements. The IMARPE in situ sampling seemed sufficient to reproduce the SST temporal variability near the coast, while for ZT, ZNO$_3$, and surface Chl a denser sampling would be needed.

### 4.2. Seasonal Response of Chlorophyll During EN

During neutral periods, Chl concentration presented a marked seasonality driven by nutrient and light limitation growth factors. Nutrient and light limitation were quantified by computing the limitation terms offline [see *Echevin et al.*, 2008; *Aumont et al.*, 2015, for details]. In the nearshore mixed layer, strong nutrient limitation ($\sim$0.2–0.4) was found during late spring-summer and strong light limitation ($\sim$0.2) during winter (Figure 15a). Nutrient limitation showed a marked seasonality with nitrate limitation during spring-summer and iron limitation during autumn-winter (Figures 15b and 15c). Using a regional model setting similar to ours, *Echevin et al.* [2008] suggested that iron limitation could occur during winter, in line with *Messié and Chavez* [2015] results based on in situ and satellite observations.

The seasonality of limiting factors did not change during EN. However, slightly enhanced light limitation in summer and nutrient (nitrate) limitation in winter were found during EN with respect to neutral periods (Figure 15a). The nutrient limitation increase was related to the nitrate vertical flux decrease in winter, while it was compensated by the upwelling increase in summer (Figures 9e and 9f). On the other hand, the light limitation increase during EN in summer can be explained by the ML deepening (supporting information Figure S3). To investigate the impact of the model nitrate bias on these results, the light and nutrient limitation terms were computed in a different model run (named RPOrca, see details in supporting information) which simulated a reduced nitrate content. It reproduced the nitrate decrease during EN in the same proportion as the simulation analyzed in the previous sections (supporting information Figure S4a). However, in summer during EN, nutrient limitation was enhanced, whereas light limitation was not changed due to a weak wind increase (supporting information Figure S4b). Thus, our conclusion is that both light and nutrient limitation may play a role in the decrease of Chl during EN, depending on the nutrient subsurface concentration and mixed layer variability.

### 4.3. Onshore Surface Geostrophic Transport During EN

Using satellite observations, *Thomas et al.* [2009] found strong negative anomalies of Chl concentration during the 1997–1998 EN in the Peru and California systems. They mentioned that the anomalies were
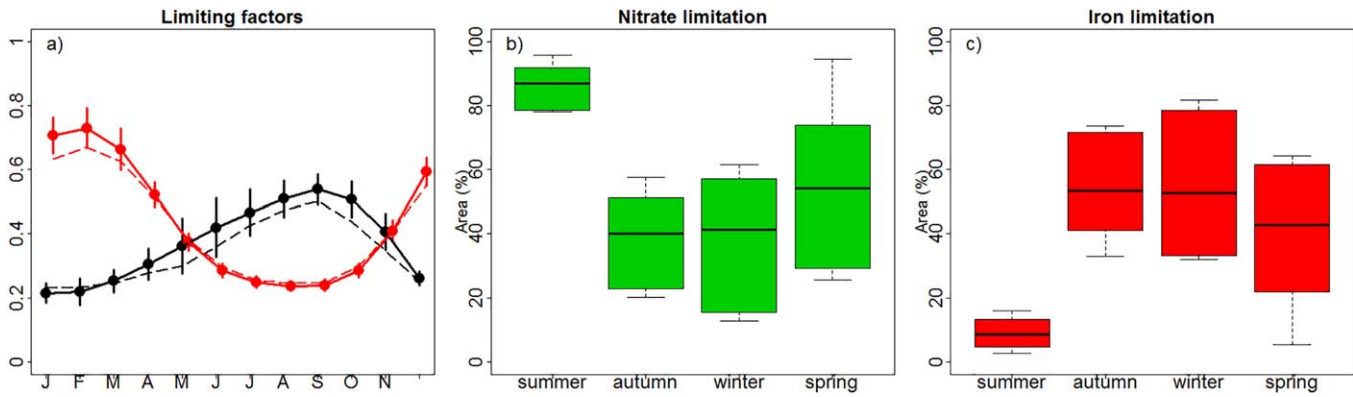
**Figure 15.** (a) Seasonal cycle of diatoms growth limiting factors during EN (dashed line) and neutral period (thick line). Light limitation is marked in red; nutrient in black. Error bars represent standard deviation. Values were averaged in the mixed layer and in a coastal band. Values close to 1 indicate weak limitation. Seasonal cycle of (b) nitrate and (c) iron limitation for diatoms. The % of limitation was computed as the ratio between the number of pixels with nutrient (nitrate or iron) limitation and the total number of pixels in the coastal band (see Figure 1).

associated with both negative and positive wind-driven upwelling anomalies, but also that anomalous subsurface hydrographic structures may change the canonical relationship between upwelling, nutrient flux and Chl response. In spite of the wind increase during EN [e.g., *Bakun et al.*, 1973; *Enfield*, 1981; *Bakun et al.* 2010; *Kessler*, 2006], a positive correlation between coastal upwelling and alongshore wind stress was only found during summer-early autumn. During the rest of the year, our model reproduced an upwelling decrease despite the wind stress intensification, due to a compensation of the upwelling by an onshore geostrophic flow [*Colas et al.*, 2008; *Marchesiello and Estrade*, 2010]. *Carr et al.* [2002] computed an upwelling index based on the difference between coastal and oceanic SST, which indicated a decrease in upwelling during El Nino north of 15°S. The shutdown of the upwelling during EN was also mentioned by *Zuta and Guillén* [1970], and by *Huyer et al.* [1987] from the observation of cross-shore sections of temperature during 1982–1983 at 10°S.

The decoupling between upwelling-favorable winds and vertical flux during EN was studied by *Huyer et al.* [1987] and by *Colas et al.* [2008]. They showed that the enhanced wind-driven upwelling during EN was partly compensated by an onshore geostrophic flow driven by an alongshore sea-level gradient. To document this process in our simulation, we computed the zonal geostrophic current ($u_g$) at ∼200 km from the coast between 6°S and 16°S and compared it with the surface $u_g$ derived from AVISO data. The zonal geostrophic current presented positives anomalies not only during the 1982–1983 and 1997–1998 events but also during the other EN events in the simulation period (Figure 16a). The compensating current was strong in winter and spring, and weaker or nonexistent in summer (Figure 16b). This explains the EN positive vertical flux forced by enhanced upwelling-favorable winds in summer (Figures 9a and 9c).
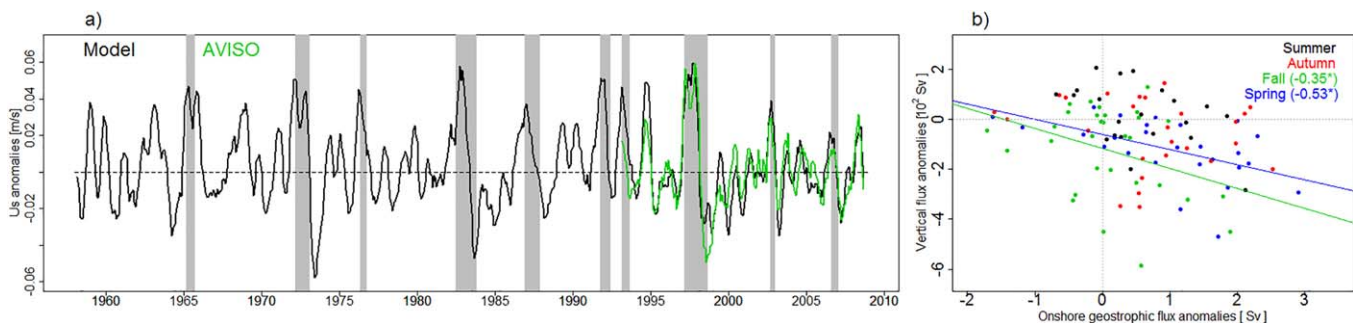


**Figure 16.** Time series of geostrophic zonal surface currents (in m.s$^{-1}$) derived from the model (black line) and AVISO (green line) sea level. (a) Spatial averaging was performed between 6°S–16°S and 150–200 km from the coast. (b) Scatterplot of the monthly vertical flux anomalies (at 20 m depth) and onshore geostrophic flux anomalies (for 20 m thick surface layer) during EN. Colors and lines represent seasons and significant linear regression, respectively.

#### 4.4. Changes in SW During EN

Using a simplified one-dimensional model, *Carr* [2003] hypothesized that the wind-driven upwelling increase during EN may induce a SW deepening and stimulate favorably planktonic growth. In contrast, our results suggested that the SW depth near the upwelling region (e.g., 1 month before they are upwelled) did not exhibit significant changes during EN, in line with *Huyer et al.* [1987].

However, SW characteristics were modified in the equatorial region (88°W), months before being upwelled. During moderate EN events, the SW nutrient content and depth were not significantly different from those during the neutral period, while during extreme events SW were shallower and nutrient-poorer. These differences are likely to be related to the different duration of EN periods as well as regional circulation changes. As a moderate EN event spanned on average ∼8 months, the SW at 88°W did not undergo a depressed nutricline typical of EN conditions in the equatorial region, because at the time of their departure from the equatorial region the event had not developed yet. Thus SW encountered a deep nutricline only in the nearshore region during the passage of the CTW. In contrast, during an extreme, much longer (∼16 months) EN event, SW transited much more rapidly from 88°W to the upwelling region, and their characteristics (e.g., low nutrient due to a anomalously deep nutricline) were modified in the equatorial region as EN conditions (e.g., deeper nutricline) had fully developed.

#### 4.5. Eddy-Driven Nutrient Subduction During EN

Mesoscale turbulence generated by the alongshore currents instabilities modulates nearshore turbulent fluxes of nutrients and plankton in upwelling systems [e.g., *Lathuilière et al.*, 2010; *Gruber et al.*, 2011; *Renault et al.*, 2016]. Using an eddy-resolving biophysical coupled model coupled in the California Current System, *Gruber et al.* [2011] evidenced coastal nitrate loss by eddy-driven offshore transport and subduction. This process reduces the nearshore primary production due to offshore and downward transport of phytoplankton and upwelled nutrients. In particular, the net effect of downward eddy flux in the offshore region is to deplete the upwelling SW and thus to reduce the coastal productivity. Offshore transport of nutrients within eddy cores [*Stramma et al.*, 2013] and subduction of newly upwelled in submesoscale cold filaments [*Thomsen et al.*, 2016] were previously evidenced in the PCUS. Our results show that the percentage of the nitrate vertical eddy flux with respect to the mean vertical nutrient flux increased during EN. However, the magnitude of the nitrate vertical eddy flux could be underestimated due to the relatively low horizontal resolution (1/6°) of our model [e.g., *Capet et al.*, 2008; *Colas et al.*, 2012]. An underestimated subduction in our simulation could partly explain the overly high surface Chl (Figures 3p and 3q).

Note that in spite of its relatively low resolution, our model represented correctly the spatial (supporting information Figure S5) and interannual (Figure 12a) variability of the EKE. A resolution of 1/6° is eddy-resolving off Peru due to its proximity to the equator, as the typical length scale of mesoscale structures would be covered by ∼10 grid points [*Belmadani et al.*, 2012]. Nevertheless, more modeling studies with an increased spatial resolution would be needed to better understand and quantify the role of submesoscale variability on surface productivity off Peru.

### 5. Conclusions

The main physical and biogeochemical processes acting on the development of phytoplankton biomass off Peru during EN were studied using a three-dimensional, eddy-resolving, coupled physical-biogeochemical regional model, evaluated with in situ and satellite observations. The model was able to reproduce the main characteristics of several EN events (extreme and moderate) occurring between 1958 and 2008: the temperature and sea level increase, the thermocline/nutricline deepening, and the phytoplankton (mainly diatoms) and nutrient concentration decrease along the Peruvian coast.

During EN periods, coastal upwelling intensified (mainly in summer-fall) due to a nearshore wind stress increase, but was partly compensated by an onshore geostrophic flow associated with an alongshore sea-level gradient in winter and spring. CTW propagating along the coast increased dramatically the depth of thermocline and nutricline, particularly in late spring-early summer. Consequently, the nitrate vertical flux into the surface layer decreased, except in summer-early autumn when the subsurface nitrate decrease was mitigated by the wind-driven upwelling increase. In our simulations, the Chl decrease during summer was

thus mainly attributed to an increase of light limitation related with a deepening of the mixed layer, while it was caused by nutrient depletion during the other seasons.

The nutrient (nitrate and iron) content of the upwelling source waters strongly decreased in summer-autumn in the region of upwelling during EN, while their depth was little modified. In the equatorial region away from the coasts, the source water properties did not change during neutral, EN moderate, and LN periods, while during extreme EN events their nutrient content was lower (20%) in relation to the longer duration of these events. This sequence of events could be modified under intensified surface warming (e.g., related to regional climate change) as the annual mean upwelling intensity could decrease and source waters may shoal due to much stronger changes in stratification than those occurring during EN [*Oerder et al.* 2015].

The impact of EN events depended of their intensity. Extreme EN affected the structure of the water column and the Chl surface concentration more than moderate events. The impact of LN was opposite and much weaker than the impact of EN.

During EN events mesoscale turbulence was stronger, which played a significant role in nutrient offshore transport and subduction. The nitrate vertical eddy flux with respect to the mean vertical nutrient flux increased during EN and was estimated in our simulation to be twice as large as during normal years. This could however be a lower bound considering the relatively low horizontal resolution of the model. A more accurate assessment of the role of eddy fluxes during EN will be performed in future work.

## References

Albert, A., V. Echevin, M. Lévy, and O. Aumont (2010), Impact of nearshore wind stress curl on coastal circulation and primary productivity in the Peru upwelling system, *J. Geophys. Res.*, *115*, C12033, doi:10.1029/2010JC006569.

Alheit, J., and M. Ñiquen (2004), Regime shifts in the Humboldt Current ecosystem, *Prog. Oceangr.*, *60*, 201–222, doi:10.1016/j.pocean.2004.02.006.

Arntz, W. E., V. A. Gallardo, D. Gutíerrez, E. Isla, L. A. Levin, J. Mendo, C. Neir, G. T. Rowe, J. Tarazona, and M. Wolff (2006), El Nino and similar perturbation effects on the benthos of the Humboldt, California, and Benguela Current upwelling ecosystems, *Adv. Geosci.*, *6*, 243–265.

Aumont, O., and L. Bopp (2006), Globalizing results from ocean in situ iron fertilization studies. *Global Biogeochem. Cycles*, *20*, GB2017, doi: 10.1029/2005GB002591.

Aumont, O., C. Ethé, A. Tagliabue, L. Bopp, and M. Gehlen (2015), PISCES-v2: An ocean biogeochemical model for carbon and ecosystem studies, *Geosci. Model Dev.*, *8*, 2465–2513, doi:10.5194/gmd-8-2465-2015.

Ayón, P., M. I. Criales-Hernandez, R. Schwamborn, and H. -J. Hirche (2008a), Zooplankton research off Peru: A review, *Prog. Oceanogr.*, *79*, 238–255, doi:10.1016/j.pocean.200810.020.

Ayón, P., G. Swartzman, A. Bertrand, M. Gutiérrez, and S. Bertrand (2008b), Zooplankton and forage fish species off Peru: Large-scale bottom-up forcing and local-scale depletion, *Prog. Oceanogr.*, *79*, 208–214, doi:10.1016/j.pocean.200810.023.

Bakun, A. (1973), Coastal upwelling indices, west coast of North America, 1946–71, *NOAA Tech. Rep., NMFS SSRF-671*, 103 pp., U.S. Dep. of Commer., Wash.

Bakun, A., D. B. Field, A. Redondo-Rodriguez, and S. J. Weeks (2010), Greenhouse gas, upwelling-favorable winds, and the future of coastal ocean upwelling ecosystems, *Global Change Biol.*, *16*, 1213–1228, doi:10.1111/j.1365-2486.2009.02094.x.

Barber, R. T., and F. P. Chavez (1983), Biological consequences of El Niño, *Science*, *222*, 1203–1210, doi:10.1126/science.222.4629.1203.

Belmadani, A., V. Echevin, B. Dewitte, and F. Colas (2012), Equatorially forced intraseasonal propagations along the Peru–Chile coast and their relation with the nearshore eddy activity in 1992–2000: A modeling study, *J. Geophys. Res.*, *117*, C04025, doi:10.1029/2011JC007848.

Bouchón, M., and C., Peña (2008), Impactos de los eventos La Niña en la pesquería peruana, *Inf. Inst. Mar Perú.*, *35*(3), 193–198.

Bruland, K. W., E. L. Rue, G. J. Smith, and G. R. DiTullio (2005), Iron, macronutrients and diatom blooms in the Peru upwelling regime: Brown and blue waters of Peru, *Mar. Chem.*, *93*, 81–103.

Buitenhuis, E., C. Le Quéré, O. Aumont, G. Beaugrand, A. Bunker, A. Hirst, T. Ikeda, T. O'Brien, S. Piontkovski, and D. Straile (2006), Biogeochemical fluxes through mesozooplankton, *Global Biogeochem. Cycles*, *20*, GB2003, doi:10.1029/2005GB002511.

Calienes, R. (2014), Producción primaria en el ambiente marino en el Pacífico sudeste, Perú, 1960–2000, *Bol. Inst. Mar Perú*, *29*(1–2), 232–288.

Carr, M.-E. (2003), Simulation of carbon pathways in the planktonic ecosystem off Peru during the 1997–1998 El Niño and La Niña, *J. Geophys. Res.*, *108*(C12), 3380, doi:10.1029/1999JC000064.

Carr, M.-E., P. T. Strub, A. C. Thomas, and J. L. Blanco (2002), Evolution of 1996–1999 La Niña and El Niño conditions off the western coast of South America: A remote sensing perspective, *J. Geophys. Res.*, *107*(C12), 3236, doi:10.1029/2001JC001183.

Capet, X., J. C. McWilliams, M. J. Molemaker, and A. F. Shchepetkin (2008), Mesoscale to submesoscale transition in the California Current System. Part I: Flow structure, eddy flux, and observational tests, *J. Phys. Oceanogr.*, *38*(1), 29–43.

Capet, X. J., P. Marchesiello, and J. C. McWilliams (2004), Upwelling response to coastal wind profiles, *Geophys. Res. Lett.*, *31*, L13311, doi: 10.1029/2004GL02123.

Carton, J. A., and B. Giese (2008), A Reanalysis of Ocean Climate Using Simple Ocean Data Assimilation (SODA), *Mon. Weather Rev.*, *136*, 2999–3017.

Casey, K. S., T. B. Brandon, P. Cornillon, and R. Evans (2010), The past, present and future of the AVHRR Pathfinder SST Program, in *Oceanography from Space: Revisited*, edited by V. Barale, J. F. R. Gower, and L. Alberotanza, Springer, Dordrecht, Heidelberg, London, New York, doi:10.1007/978-90-481-8681-5_16.

Chaigneau, A., G. Arnaud Gizolme, and C. Grados (2008), Mesoscale eddies off Peru in altimeter records: Identification algorithms and eddy spatio-temporal patterns, *Prog. Oceanogr.*, *79*, 106–119, doi:10.1016/j.pocean.2008.10.013.

Chavez, F., and M. Messié (2009), A comparison of Eastern Boundary Upwelling Ecosystems, *Prog. Oceanogr.*, *83*, 80–96, doi:10.1016/j.pocean.2009.07.032.

Chavez, F., A. Bertrand, R. Guevara-Carrasco, P. Soler, and J. Csirke (2008), The northern Humboldt Current System: Brief history, present status and a view towards the future, *Prog. Oceanogr.*, *79*, 95–105, doi:10.1016/j.pocean.2008.10.012.

Colas, F., X. Capet, J. C. McWilliams, and A. Shchepetkin (2008), 1997–98 El Niño off Peru: A numerical study, *Prog. Oceanogr.*, *79*, 138–155.

Colas, F., J. C. McWilliams, X. Capet, and J. Kurian (2012), Heat balance and eddies in the Peru-Chile current system, *Clim. Dyn.*, *39*, 509–529, doi:10.1007/s00382-011-1170-6.

Colas, F., X. Capet, J. C. McWilliams, and Z. Li (2013), Mesoscale eddy buoyancy flux and eddy-induced circulation in eastern boundary currents, *J. Phys. Oceanogr.*, *43*, 1073–1095, doi:10.1175/JPO-D-11-0241.

Conkright, M., R. Locarnini, H. Garcia, T. D. O'Brien, T. P. Boyer, C. Stephens, and J Antononov (2002), World Ocean Atlas 2001: Objectives, analyses, data statistics and figures [CD-ROM], *NOAA Atlas NESDIS 42*, Int. Report 17, Silver Spring, Md.

Da Silva, A. M., C. C. Young, and S. Levitus (1994), Atlas of surface marina data 1994, technical report, Natl. Oceanogr. And Atmos. Admin, Silver Spring, Md.

Echevin, V., O. Aumont, J. Ledesma, and G. Flores (2008), The seasonal cycle of surface chlorophyll in the Peruvian upwelling system: A model study, *Prog. Oceanogr.*, *79*, 167–176.

Echevin, V., F. Colas, A. Chaigneau, and P. Penven (2011), Sensitivity of the Northern Humboldt Current System nearshore modeled circulation to initial and boundary conditions, *J. Geophys. Res.*, *116*, C07002, doi:10.1029/2010JC006684.

Echevin, V., A. Albert, M. Lévy, O. Aumont, M. Graco, and G. Garric, (2014), Remotely-forced intraseasonal variability of the Northern Humboldt Current System surface chlorophyll using a coupled physical-ecosystem model, *Cont. Shelf Res.*, *73*, 14–30, doi:10.1016/j.csr.2013.11.015.

Enfield, D. B. (1981), Thermally driven wind variability in the planetary boundary layer above Lima, Peru, *J. Geophys. Res.*, *86*(C3), 2005–2016, doi:10.1029/JC086iCO3p02005.

Goubanova, K., V. Echevin, B. Dewitte, F. Codron, K. Takahashi, P. Terray, and M. Vrac (2011), Statistical downscaling of sea-surface wind over the Peru-Chile upwelling region: Diagnosing the impact of climate change from the IPSL-CM4 model, *Clim. Dyn.*, *36*, 1365, doi:10.1007/s00382-010-0824-0.

Graco, M., J. Ledesma, G. Flores, and M. Girón (2007), Nutrientes, oxígeno y procesos biogeoquímicos en el sistema de surgencias de la corriente de Humboldt frente a Perú, *Rev. Per. Biol.*, *14*(1), 117–128.

Graco, M., S. Purca, B. Dewitte, O. Morón, J. Ledesma, G. Flores, C. Castro, and D. Gutiérrez (2016), The OMZ and nutrients features as a signature of interannual and low frequency variability off the peruvian upwelling system, *Biogeosci. Discuss.*, doi:10.5194/bg-2015-567, in press.

Gruber, N., Z. Lachkar, H. Frenzel, P. Marchesiello, M. Munnich, J. McWilliams, T. Nagai, and G. Plattner (2011), Eddy-induced reduction of biological production in eastern boundary upwelling systems, *Nat. Geosci.*, *4*, 787–792.

Gutiérrez, D., et al. (2011), Coastal cooling and increased productivity in the main upwelling zone off Peru since the mid-twentieth century, *Geophys. Res. Lett.*, *38*, L07603, doi:10.1029/2010GL046324.

Gutiérrez, D., M. Akester, and L. Naranjo (2016), Productivity and Sustainable Management of the Humboldt Current Large Marine Ecosystem under climate change, *Environ. Dev.*, *17*, 126–144, doi:10.1016/j.envdev.2015.11.004.

Halpern, D. (2002), Offshore Ekman transport and Ekman pumping off Peru during the 1997–1998 El Niño, *Geophys. Res. Lett.*, *29*(5), 1075, doi:10.1029/2001GL014097.

Hernandez, O., P. Lehodey, I. Senina, V. Echevin, P. Ayón, A. Bertrand, and P. Gaspar (2014), Understanding mechanisms that control fish spawning and larval recruitment: Parameter optimization of an Eulerian model (SEAPODYM-SP) with Peruvian anchovy and sardine eggs and larvae data, *Prog. Oceanogr.*, *123*, 105–122.

Huang, B., V. F. Banzon, E. Freeman, J. Lawrimore, W. Liu, T. C. Peterson, T. M. Smith, P. W. Thorne, S. D. Woodruff, and H. -M. Zhang (2015), Extended Reconstructed Sea Surface Temperature version 4 (ERSST.v4): Part I. Upgrades and intercomparisons, *J. Clim.*, *28*, 911–930, doi:10.1175/JCLI-D-14-00006.1.

Hutchins, D. A., et al. (2002), Phytoplankton iron limitation in the Humboldt Current and Peru Upwelling, *Limnol. Oceanogr.*, *47*, 997–1011, doi:10.4319/lo.2002.47.4.0997.

Huyer, A., R. L. Smith, and T. Paluszkiewicz (1987), Coastal upwelling off Peru during normal and El Niño times, *J. Geophys. Res.*, *92*(C13), 14,297–14,307, doi:10.1029/JC092iC13p14297.

Huyer, A., M. Knoll, T. Paluszkiewic, and R. L. Smith (1991), The Peru Undercurrent: A study of variability, *Deep Sea Res., Part A*, *38*, S247–S271.

Irwin, A. J., Z. B. Finkel, O. M. E.Schofield, and P. G. Falkowsky (2006), Scaling-up from nutrient physiology to the size-structure of phytoplankton communities, *J. Plankton Res.*, *28*(5), 459–471, doi:10.1093/plankt/fbi148.

Kahru, M., B. G. Mitchell, A. Diaz, and M. Miura (2004), MODIS Detects a Devastating Algal Bloom in Paracas Bay, Peru. *Eos Trans. AGU.*, *85*(45), 465–472, doi:10.1029/2004EO450002.

Kessler, W. S. (2006), The circulation of the eastern tropical Pacific: A review, *Prog. Oceanogr.*, *69*, 181–217.

Kessler, W. S., and M. J. McPhaden (1995), Oceanic equatorial waves and the 1991–1993 El Niño, *J. Clim.*, *8*, 1757–1774.

Lachkar, Z., and N. Gruber (2012), A comparative study of biological production in eastern boundary upwelling systems using an artificial neural network, *Biogeosciences*, *9*, 293–308, doi:10.5194/bg-9-293-2012.

Lathuilière, C., V. Echevin, M. Lévy, and G. Madec (2010), On the role of the mesoscale circulation on an idealized coastal upwelling ecosystem, *J. Geophys. Res.*, *115*, C09018, doi:10.1029/2009JC005827.

Lefort, S., O. Aumont O., L. Bopp, T. Arsouze, M. Gehlen, and O. Maury (2015), Spatial and body-size dependent response of marine pelagic communities to projected global climate change, *Global Change Biol.*, *21*(1), 154–164.

Liu, W., K. B. Katsaros, and J. A. Businger (1979), Bulk parameterization of the air-sea exchange of heat and water vapor including the molecular constraints at the interface, *J. Atmos. Sci.*, *36*, 1722–1735.

Marchesiello, P., and P. Estrade (2010), Upwelling limitation by onshore geostrophic flow, *J. Mar. Res.*, *68*, 37–62, doi:10.1357/002224010793079004.

McWilliams, J. C. (2016), Submesoscale currents in the ocean, *Proc. R. Soc. A*, *472*, 20160117, doi:10.1098/rspa.2016.0117.

Messié, M., and F. P. Chavez (2015), Seasonal regulation of primary production in eastern boundary upwelling systems, *Prog. Oceanogr.*, *134*, 1–18, doi:10.1016/j.pocean.2014.10.011.

Montes, I., F. Colas, X. Capet, and W. Schneider (2010), On the pathways of the equatorial subsurface currents in the eastern equatorial Pacific and their contributions to the Peru-Chile Undercurrent, *J. Geophys. Res.*, *115*, C09003, doi:10.1029/2009JC005710.

Montes, I., S. Wolfgang, F. Colas, B. Blanke, and V. Echevin (2011), Subsurface connections in the eastern tropical Pacific during La Niña 1999–2001 and El Niño 2002–2003, *J. Geophys. Res.*, *116*, C12022, doi:10.1029/2011JC007624.

Morón, O. (2000), Características del ambiente marino frente a la costa peruana, *Bol. Inst. Mar Perú*, *19*(1–2), 179–204.

Ñiquen, M., and M. Bouchón (2004), Impact of El Niño event on pelagic fisheries in Peruvian waters, *Deep Sea Res., Part II*, *51*, 563–574, doi: 10.1016/j.dsr2.2004.03.001.

Oerder, V., F. Colas, V. Echevin, F. Codron, J. Tam, and A. Belmadani (2015), Peru-Chile upwelling dynamics under climate change, *J. Geophys. Res. Oceans*, *120*, 1152–1172, doi:10.1002/2014JC010299.

OReilly, J. E., S. Maritorena, B. G. Mitchell, D. A. Siegel, K. L. Carder, S. A. Garver, M. Kharu, and C. McClain (1998), Ocean color chlorophyll algorithms for SeaWIFS, *J. Geophys. Res.*, *103*(C11), 24,937–24,953, doi:10.1029/98JC02160.

Paulmier, A., D. Ruiz-Pino, V. Garçon, and L. Farías (2006), Maintaining of the Eastern South Pacific Oxygen Minimum Zone (OMZ) off Chile, *Geophys. Res. Lett.*, *33*, L20601, doi:10.1029/2006GL026801.

Pennington, J. T., K. L. Mahoney, V. S. Kuwahara, D. D. Kolver, R. Calienes, and F. P. Chavez (2006), Primary production in the eastern tropical Pacific: A review, *Prog. Oceanogr.*, *69*, 285–317, doi:10.1016/j.pocean.2006.03.012.

Penven, P., P. Marchesiello, L. Debreu, and J. Lefèvre (2008), Software tools for pre- and post-processing of oceanic regional simulations, *Environ. Modell. Software*, *23*, 660–662, doi:10.1016/j.envsoft.2007.07.004.

Picaut, J., M. Ioualalen, C. Menkes, T. Delcroix, and M. J. McPhaden (1996), Mechanisms of the zonal displacements of the Pacific warm pool: Implications for ENSO, *Science*, *274*, 1486–1489, doi:10.1126/science.274.5292.1486.

Picaut J., E. Hackert, A. J. Busalacchi, R. Murtugudde and G. S. E. Lagerloef (2002), Mechanisms of the 1997–1998 El Niño–La Niña, as inferred from space-based observations, *J. Geophys. Res.*, *107*(C5), 3037, doi: 10.1029/2001JC000850.

Renault, L., C. Deutsch, J. C. McWilliams, H. Frenzel, J.-H. Liang, and F. Colas (2016), Partial decoupling of primary productivity from upwelling in the California Current system, *Nature*, *46*, 273–289.

Ridgway, K. R., J. R. Dunn, and J. L. Wilkin (2002), Ocean interpolation by four-dimensional least squares-Application to the waters around Australia, *J. Atmos. Oceanic Technol.*, *19*(9), 1357–1375.

Risien, C. M., and D. B. Chelton (2008), A Global Climatology of Surface Wind and Wind Stress Fields from Eight Years of QuikSCAT Scatterometer Data, *J. Phys. Oceanogr.*, *38*, 2379–2413.

Sánchez, S. (2000), Variación estacional e interanual de la biomasa fitoplanctónica y concentraciones de clorofila frente a la costa peruana durante 1976–2000, *Bol. Inst. Mar Perú*, *19*(1–2), 29–43.

Shchepetkin, A. F., and J. C. McWilliams (1998), Quasi-monotone advection schemes based on explicit locally adaptive dissipation, *Mon. Weather Rev.*, *126*, 1541–1580.

Shchepetkin, A. F. and McWilliams J.C. (2005), The regional oceanic modeling system: A split-explicit, free-surface, topography-following-coordinate ocean model, *Ocean Modell.*, *9*, 347–404.

Shchepetkin, A. F. and J. C. McWilliams (2009), Computational kernel algorithms for fine-scale, multiprocess, longtime oceanic simulations, *Handb. Numer. Anal.*, *14*, 121–183, doi: 10.1016/S1570-8659(08)01202-0.

Smith, W. H. F., and D. T. Sandwell (1997), Global sea floor topography from satellite altimetry and ship depth soundings, *Science*, *277*, 1957–1962.

Stramma, L., H. W. Bange, R. Czeschel, A. Lorenzo, and M. Frank (2013), On the role of mesoscale eddies for the biological productivity and biogeochemistry in the eastern tropical Pacific Ocean off Peru, *Biogeosciences*, *10*, 7293–7306, doi:10.5194/bg-10-7293-2013.

Sunda, W. G., and S. A. Huntsman (1997), Interrelated influence of iron, light and cell size on marine phytoplankton growth, *Nature*, *390*, 389–392.

Takahashi, K., A. Montecinos, K. Goubanova, and B. Dewitte (2011), ENSO regimes: Reinterpreting the canonical and Modoki El Niño, *Geophys. Res. Lett.*, *38*, L10704, doi:10.1029/2011GL047364.

Tam, J., et al. (2008), Trophic modeling of the Northern Humboldt Current Ecosystem, Part I: Comparing trophic linkages under La Niña and El Niño conditions, *Prog. Oceanogr.*, *79*, 352–365, doi:10.1016/j.pocean.2008.10.007.

Tarazona, J., and W. Arntz (2001), The Peruvian Coastal Upwelling System, *Coastal Mar. Ecosyst. Latin Am.*, *144*, 229–244, doi:10.1007/978-3-662-04482-7_17.

Thomas, A. C., M. E. Carr, and P. T. Strub (2001), Chlorophyll variability in eastern boundary currents, *Geophys. Res. Lett.*, *28*(18), 3421–3424, doi:10.1029/2001GL013368.

Thomas, A. C., P. Brickley, and R. Weatherbee (2009), Interannual variability in chlorophyll concentrations in the Humboldt and California Current Systems, *Prog. Oceanogr.*, *83*, 386–392, doi:10.1016/j.pocean.2009.07.020.

Thomsen, S., T. Kanzow, F. Colas, V. Echevin, G. Krahmann, and A. Engel (2016), Do submesoscale frontal processes ventilate the oxygen minimum zone off Peru?, *Geophys. Res. Lett.*, *43*, 8133–8142, doi:10.1002/2016GL070548.

Tovar, H., and D. Cabrera (1985), Las aves guaneras y el fenómeno ''El Niño'', in *El fenómeno ''El Niño'' y su impacto en la fauna marina, extraordinary* vol. 181–186, edited by W. F. Arntz, A. Landa, and J. Tarazona, Bol. Inst. Mar Perú, Callao, Peru.

Travers, M., Y. J. Shin, S. Jennings, E. Machu, J. A. Huggett, J. G. Field, and P. Cury (2009), Two-way coupling versus one-way forcing of plankton and fish models to predict ecosystem changes in the Benguela, *Ecol. Modell.*, *220*(21), 3089–3099, doi:10.1016/j.ecolmodel.2009.08.016.

Tsuchiya, M. (1975), Subsurface countercurrents in the eastern equatorial Pacific, *J. Mar. Res.*, *33*, 145–175.

Ulloa, O., R. Escribano, S. Hormazabal, R. A. Quiñones, R. R. González, and M. Ramos (2001), Evolution and biological effects of the 1997–98 El Niño in the upwelling ecosystem off northern Chile, *Geophys. Res. Lett.*, *28*(8), 1591–1594, doi:10.1029/2000GL011548.

Uppala, S. M., et al. (2005), The ERA-40 re-analysis, *Q. J. R. Meteorol. Soc.*, *131*, 2961–3012, doi:10.1256/qj.04.176.

Wood, R., et al. (2011), The VAMOS Ocean-Cloud-Atmosphere-Land Study Regional Experiment (VOCALS-REx): Goals, platforms, and field operations, *Atmos. Chem. Phys.*, *11*(2), 627–654, doi:10.5194/acp-11-627-2011.

Wyrtki, K (1967), Circulation and water masses in the eastern equatorial Pacific Ocean, *Int. J. Oceanol. Limnol.*, *1*, 117–147.

Zuta, S., and O. G. Guillén (1970), Oceanografía de las aguas costeras del Perú, *Bol. Inst. Mar Perú*, *2*, 157–324.